Master's Thesis

IDEA LEAGUE APPLIED GEOPHYSICS: TU DELFT, ETH ZÜRICH & RWTH Aachen

Mars Reflectivity by Ambient Noise Correlation

by Kevin Growe

Supervisor: Dr. Pascal Edme [(1)]

Submission Date: 06.08.2021

[(1)] ETH Zürich, Institute of Geophysics

Contents

Abstract 4

1 Introduction 5
- 1.1 Motivation . . . 5
- 1.2 The InSight Mission . . . 5
- 1.3 The SEIS and APSS Instruments . . . 6
  - 1.3.1 SEIS . . . 6
  - 1.3.2 APSS . . . 6
- 1.4 Seismic Properties of Mars . . . 7
  - 1.4.1 Marsquakes . . . 7
  - 1.4.2 Noise on Mars . . . 7
  - 1.4.3 Constraints on the Martian Crust and upper Mantle . . . 7

2 Seismic Interferometry - Reflectivity by Autocorrelation 8

3 Raw Data 10
- 3.1 Waveform Data . . . 10
  - 3.1.1 Lander Modes . . . 12
  - 3.1.2 The 2.4 Hz Mode . . . 12

4 Pre-processing and Removal of Spurious Signals 12
- 4.1 Removal of Spurious Signals . . . 12
  - 4.1.1 Ticknoise . . . 13
  - 4.1.2 Glitches . . . 14
- 4.2 Preprocessing . . . 15
- 4.3 Supression of Lander Modes . . . 16
- 4.4 Amplitude Balancing . . . 18

5 Computation and Evaluation of Autocorrelation 19
- 5.1 Ambient Noise ACs . . . 19
- 5.2 Marsquake ACs . . . 20
- 5.3 Phase Weighted Nonlinear Stacking . . . 20

6 Results from Autocorrelation 21
- 6.1 Ambient Noise ACs . . . 22
- 6.2 Marsquake ACs . . . 25
- 6.3 Comparison AACs & MACs . . . 26
- 6.4 Removing the 2.4 Hz Mode . . . 28

7 Discussion 28
- 7.1 Influence of Spurious Signals and Lander Modes . . . 28
  - 7.1.1 Lander Modes . . . 28
  - 7.1.2 Remaining Glitches and Ticknoise . . . 29
- 7.2 The 2.4 Hz Resonance . . . 30
- 7.3 Comparison of Results with Previous Studies . . . 30
- 7.4 Potential Layer Interfaces . . . 31

8 Conclusion and Outlook **32**

Acknowledgements **33**

References **34**

Appendix **39**

Supplementary Material **41**

List of Figures

1 InSight lander & landing site . . . 6
2 Concept of Seismic Interferometry . . . 9
3 Raw Data . . . 11
4 Ticknoise removal . . . 14
5 Glitch removal . . . 15
6 Spectrograms of Martian evening . . . 17
7 Spectrograms after filtering . . . 18
8 Amplitude balancing . . . 19
9 Filtered ACs-Z . . . 23
10 Ambient noise ACs for the N-component, narrow band . . . 23
11 Ambient noise ACs for the E-component, narrow band . . . 24
12 Marsquake ACs: component-Z . . . 25
13 Filtered Event ACs: north component . . . 26
14 Filtered Event ACs: east component . . . 26
15 Compilation of AAC & MAC stacks . . . 27
16 ACs-Z with bandstop in 2.4 Hz . . . 28
A1 Reflection & Transmission . . . 39
S1 Brute ACs . . . 41
S2 Compilation of different PWS approaches . . . 41
S3 Filtered ACs-Z, BP: 0.3-3.2 Hz . . . 42
S4 Filtered ACs-N . . . 42
S5 Filtered ACs-E . . . 43
S6 ACs all, Z . . . 43
S7 ACs waste . . . 44
S8 Instrument response removal . . . 45

List of Tables

1 Suppression of lander modes . . . 16
2 Marsquakes used for ACs . . . 20

Abstract

In the end of November 2018 the InSight mission landed on the Martian surface deploying a six axis broadband and short period seismometer, in order record marsquakes and ambient noise, which can be used to constrain the deeper interior structures of the planet. In this study we process the three components of the broad band seismometer and apply autocorrelation methods to more than a year of ambient noise data and to 250 selected marsquake waveforms, to retrieve the empirical Greens functions (EGFs), that are related to the subsurface impedance discontinuities below the lander. The most prominent impedance discontinuity is commonly represented by the crust-mantle boundary (Moho), which yet needs to be confirmed on Mars. A lot of care is taken to attenuate the spurious signals and the wind induced lander resonance, that contaminate the data, before the autocorrelation analysis. We further apply attribute filtering and reject data windows that exceed wind speed thresholds or reveal too large amplitudes at later lags, which are often related to residuals of artefacts or lander resonance. To further improve the signal to noise ratio of the EGFs we apply phase-weighted stacking. We observe a good agreement in the autocorrelograms of the ambient noise and the marsquakes and determine several stable arrivals on the vertical component, in particular at 10.8 and 12.7 s, that we interpret as trapped P-waves, which are reflected between the surface and the potential Moho or other layer interfaces. Using available velocity constraints we convert the arrival times to possible Moho depths of 19-28 and 22-33 km, respectively. In addition, we find that large part of the seismic energy during the quiet night period of Mars is related to the 2.4 Hz mode and that removing it from the autocorrelations the distinct arrivals can no longer be identified.

1 Introduction

1.1 Motivation

The structural layering of a planet provides a glimpse into its formation and evolution. The main interior structures and discontinuities of Mars are yet to be determined. Just recent work using seismic interferometry methods and receiver functions as well as analysis of the major detected marsquakes provided new insights of an inter-crustal layer, the Moho as well as deeper interfaces.
On earth, where many seismic sensors are combined to arrays and arrays are merged to global networks, usually data of large ensembles of sensors is inverted jointly to constrain subsurface structures. As there is currently only one station available on the surface of Mars, the scientific community is confined to single station based methods to infer subsurface properties of the planet. In this study we use ambient noise and marsquake autocorrelation to extract trapped P- and S-waves from the ambient wavefield that propagate vertically below the InSight lander and reflect between subsurface layers and the surface. Using available velocity information, we can then infer the potential layer depths below the station.

1.2 The InSight Mission

The InSight mission (Interior exploration using Seismic Investigations, Geodesy and Heat Transport) launched on 5th May 2018 from Vandenberg Air Force Base in Califonia and landed, after a six-month cruise, on November 26. 2018 successfully in Elysium Planitia on the Martian surface (*NASA*, 2021a; *Banerdt* et al., 2020). The landing site is located at 4.5° north latitude and 135.9° east longitude (*Golombek* et al., 2017) in a rather flat area providing a smooth surface for the stable landing and an unproblematic deployment of the solar panels (*NASA*, 2021a;Fig.1b). The proximity to the equator was chosen to produce enough solar power for the operating instruments and the heating system to keep the lander warm throughout the entire martian year, which is currently challenged by the harsh martian winter and the dust cover on the solar panels (*NASA*, 2021b).
The overall goal of the mission is to study the planets interior structure, composition and thermal state using marsquake and impact events as well ambient noise data. To achieve this goal the lander features multiple scientific modules for measuring the ground vibrations as well as a variety of of atmospheric, and telemetric parameters (*NASA*, 2021a).

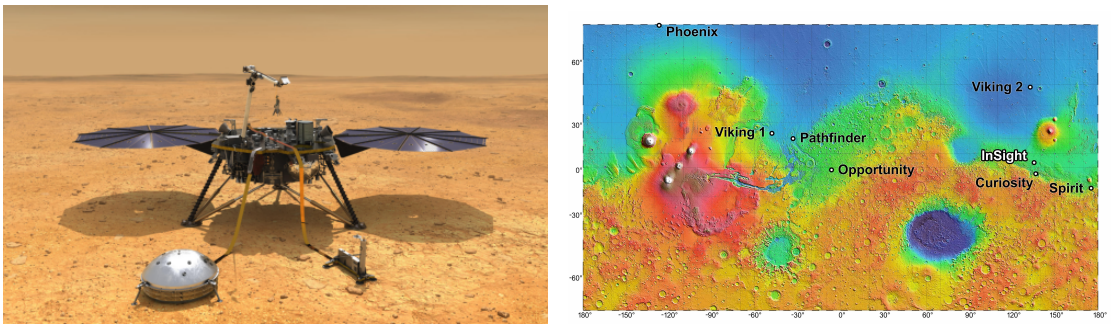

(a) (b)

Figure 1: (a) Visualization of the InSight lander on the martian surface with deployed SEIS instrument protected with a wind and thermal shield, the mole of the HP^3 module and solar arrays. (b) Topographic map of Mars showing the landing sites of the InSight lander as well as the landers and rovers of previous Mars missions. Topographic data is obtained from the Mars Orbiter Laser Altimeter on NASA's Mars Global Surveyor spacecraft. The elevation is mapped with respect to a reference datum since there is no existing sea level on Mars. Darkblue and white indicate the lowest and highest topography, respectively (*NASA*, 2021a). Mars' topography thereby ranges from -8 to +12 km with respect to the reference datum (*Golombek* et al., 2020, Fig.1). Image courtesy: NASA/JPL-Caltech (`https://mars.nasa.gov/insight/multimedia/images/`)

1.3 The SEIS and APSS Instruments

1.3.1 SEIS

The SEIS instrument (Seismic Experiment for Interior Structure), contains six ground motion sensors of which three are very broadband sensors (VBB) and measure periods from tidal up to 0.1 s, whereas the other three are short period (SP) sensors that measure frequencies from 0.1 up to 50 Hz (*Lognonné* et al., 2019; *Lognonné* et al., 2020). The axis are obliquely oriented (e.g. *Ceylan* et al., 2020) and need to be rotated to the true geographic orientations. The true north was determined by *Savoie* et al. (2021). In order to protect the SEIS instrument from the rough martian temperatures and to reduce the environmental noise level, it is covered by a wind- and thermal shield (Fig. 1). The instrument was placed on the martian surface by a robotic arm and is connected with a tether to the lander. The tether contains an anti-vibration unit to mitigate the tether induced noise on the SEIS data (*Lognonné* et al., 2019). The acquired data is stored on the lander, transmitted to the mars orbiter and redirected to earth where it is reviewed, archived and published (*Insight Mars SEIS Data Service*, 2019). Due to the limited bandwidth, only the 20 samples per second (sps) channel is available for most of the acquisition period. The 100 sps data is only transmitted on request (e.g. to resolve events).

1.3.2 APSS

The APSS (Auxiliary Payload Sensor Suit) contains sensors that measure atmospheric parameters: wind speed and direction, air temperature, and atmospheric pressure. In-

strument specifications can be obtained in *Banfield* et al. (2019). The monitoring of atmospheric parameters is crucial to understand the environmental noise that affect the SEIS data. In this study we make use of the wind speed data, which is measured with two different booms at different location on the deck. The wind data is downloaded from NASA's PDS. Here, we use the derived data which is composite data combining both wind sensors. The wind data is generally affected by many gaps, that we interpolate.

1.4 Seismic Properties of Mars

1.4.1 Marsquakes

The SEIS data is continuously monitored for marsquakes and other events by the Marsquake Service (MQS; *InSight Marsquake Service*, 2021; *Clinton* et al., 2021. Since the beginning of the InSight mission, the MQS has detected and published ∼1300 events (*InSight Marsquake Service*, 2021), revealing an active seismic planet. The marsquake events can be categorized in terms of their frequency content and signal to noise ratio ratio (SNR) (*Clinton* et al., 2021). Their frequency content range from between 0.1 and 1 Hz for low frequency events (LFs; *Giardini* et al., 2020) to frequencies between 1-10 Hz for high frequency events (*Driel* et al., 2021. The HFs can further be subdivided into HFs, 2.4 Hz events and very high frequency events (VHFs; *InSight Marsquake Service*, 2021). *Driel* et al. (2021) studied the HFs in detail and found that all events of the three HF classes excite the so-called 2.4 Hz resonance mode, which is discussed in more detail in Section 3 & 7. The authors further used spectral envelope modelling of the HFs and explain them as guided crustal phases (Pg,Sg) that experience low attenuation. Another event type, that is not considered as marsquakes, contains frequency content from 5-30 Hz, was found by *Dahmen* et al. (2020) and was classified as super high frequency events (SFs). The authors relate these events to the thermal cracking of surface- or near surface rocks in the vicinity of the lander, due to thermal expansion. Most events are recorded during the quiet night periods of the sol. A sol is a Martian day, which is ∼40 min longer than day on Earth.

1.4.2 Noise on Mars

Multiple studies have shown, that the noise level during Martian nights is extremely low at the lower frequencies around 0.03-1 Hz, up to a factor 1/500 with respect to night on Earth (*Stutzmann* et al., 2021; *Lognonné* et al., 2020). This low noise level generally allows for detection of events with 1.8 magnitudes lower than on Earth. The noise level around 1 Hz is similar to the noise level of the Moon but it is much lower for lower frequencies. There are no oceans on Mars, which represent the largest noise source on Earth. The correlation between the seismic records, the atmospheric pressure and wind data suggest that the Martian atmosphere is the main noise source, where lower frequencies are predominantly excited by ground deformation caused by pressure perturbations and higher frequencies are mostly generated by wind-induced lander noise (*Lognonné* et al., 2020).

1.4.3 Constraints on the Martian Crust and upper Mantle

Geochemical constraints using orbital Gamma Ray Spectrometry (*Baratoux* et al., 2011) and the geology (*Golombek* et al., 2020) suggest a basaltic upper crust on the Mars.

Lognonné et al. (2020) computed the first receiver functions on Mars for three major marsquakes with high SNR and found a signals at 2.2-2.4 s after the P-wave onset, that they interpret as a velocity discontinuity in 8-11 km depth, and an upper layer S-wave velocity of 1.7-2.1 km/s. A recent study from *Knapmeyer-Endrun* et al. (2021) that confirmed these results, will be discussed in more detail in Section 7. The obtained velocities result in a velocity reduction of up to 50 % compared Earth analogues (*Lognonné* et al., 2020) and thus suggest a strongly altered and fractured crust (*Smrekar* et al., 2019). *Giardini* et al. (2020) analyzed the first 174 detected marsquakes and inferred a low velocity zone within the mantle from the observed distance variation of S-wave amplitudes. More results from recent studies revealing subsurface interfaces (e.g *Knapmeyer-Endrun* et al., 2021; *Compaire* et al., 2021; *Deng* and *Levander*, 2020) are discussed jointly with our results in Section 7.

2 Seismic Interferometry - Reflectivity by Autocorrelation

Seismic interferometry methods rely on the concept of cross-correlation of two diffusive wavefield recordings from two different stations to extract the Greens function for the path between the two stations R_1 and R_2(*Campillo* and *Paul*, 2003; *Lobkis* and *Weaver*, 2001). Thus, the Greens function G_{12} represents the recording of the wavefield at station R_1 using an virtual, impulsive source at station R_2 (e.g *Wapenaar*, 2004; *Snieder*, 2004). The definition of a diffusive wavefield was established in room acoustics (*Hodgson*, 1996). Hereafter, a wavefield is diffuse if the following assumptions are valid (*Mulargia*, 2012):

1. the wavefield is a noise field and consists of purely random phases
2. the waves recorded at the receiver are coming from all directions; the wavefield is thus isotropic in azimuth
3. the wavefield is equal at a local scale, i.e. it has the same amplitude for all points in space

As in reality the wave field is generally never completely diffuse (e.g. *Mulargia*, 2012), the Greens functions can not be reconstructed perfectly and are referred to as empirical Greens functions (EGF; e.g. *Weaver* and *Lobkis*, 2005). The concept of seismic interferometry is illustrated in Figure 2 from *Edme* and *Halliday* (2016) for different travel paths of the waves. We note that, if receiver R_1 and R_2 are the same, the cross-correlation becomes the autocorrelation (AC) and the extracted EGFs are related to the subsurface impedance discontinuities (reflectivity) below the station. Hence, with the AC of the ambient diffusive wave field recorded at a station we can extract vertically propagating wave phases that reverberate in between layer interfaces in the subsurface and the station at the free surface. Stacking the ACs over a long time of recording improves the SNR and thus the EGFs. Figure 2d shows an synthetic example of a narrow band oscillatory event, that reverberates in the subsurface below the station. The 'passive' and 'virtual active' time series thereby represent the recorded trace and the corresponding AC. The arrivals for primary and multiple reflections are obtained in the AC at the lag times that correspond to the two-way traveltimes between the layer interfaces. Due to the narrow bandwidth of the event the EGFs can not be reconstructed very accurately (i.e. the arrivals in the AC contain many sidelobes), hampering the unambiguous identification of phases.

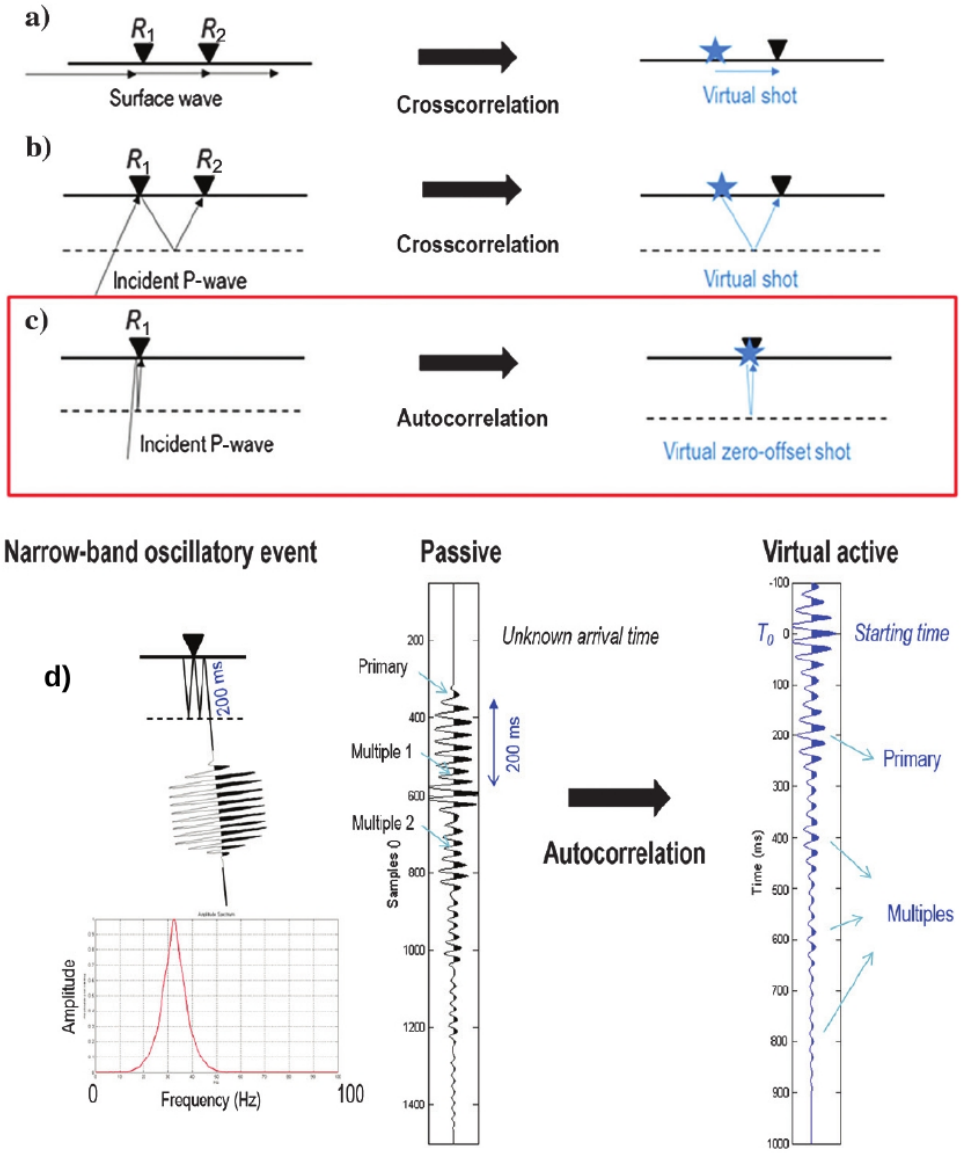

Figure 2: Conceptual sketch of seismic interferometry from *Edme* and *Halliday* (2016). **(a)** The cross-correlation of the traces of two receivers recording the wave traveling the direct path along the receivers can be expressed as a virtual shot fired at the location of the first receiver, injecting the recorded wavefield of that receiver. **(b)** The same substitution is valid for waves that first reflect from the free surface at the first receiver and reflect again from a subsurface layer before reaching the second receiver. Here, the reflected path is obtained. **(c)** If receiver 2 is equal to receiver 1, the reflected phase becomes the zero offset reflection which is then obtained by the autocorrelation of the trace. **(d)** A narrow band event impinges from below the station and reverberates in between the free surface and the subsurface interface. The trace labeled as 'passive' depicts the synthetic recording, whereas the virtual active trace represents the computed AC of the recording.

The mathematical foundation was pioneered already by *Claerbout* (1968), who showed, that the reflection response of a horizontally layered medium can be derived from the autocorrelation function of the corresponding transmission response. Thus, assuming a

source below the considered medium, the AC of the transmitted wavefield is equivalent to the injection of a virtual source at the station location and recording of the corresponding zero-offset reflection response. *Wapenaar* (2003) reviewed these findings, provided a 1D derivation using the laws of power conservation and an extension to three dimensions. A brief recap of the 1D derivations for the horizontally layered medium is provided in the appendix.
Today, ambient noise autocorrelation analysis to extract the EGFs that are representative for the subsurface reflectivity, is well established method in seismology and is used for many studies on Earth (e.g. *Gorbatov* et al., 2013; *Oren* and *Nowack*, 2016). Instead of using ambient noise, AC methods can also be applied to quake coda given that the wavefield is diffusive. Thus, AC analysis has been used for earthquake coda (e.g. *Pham* and *Tkalčić*, 2017; *Galetti* and *Curtis*, 2012), on moonquakes (e.g. *Nishitsuji* et al., 2016) and since recently also on marsquakes (e.g. *Compaire* et al., 2021).

3 Raw Data

3.1 Waveform Data

The raw data recorded by the components of the Insight Lander is stored and published in MSEED format. In the beginning of the mission the VBB data was mostly acquired with 10 Hz sampling frequency, whereas onwards from sol ∼180 the data was acquired continuously with 20 Hz. There are two channels per component and sampling frequency, with either low or high gain applied to the instrument. In this study we use all three VBB components, sampled with 20 Hz and high gain (e.g. channels BHU, BHV, BHW). The data is separated in Earth days, such that for each day on Earth a distinct MSEED file is stored for each of the components U,V,W. The meta data is stored in a dataless SEED file and contains all the crucial information including component axis orientations and instrument response. The data and meta data for all channels and the corresponding channel information can be accessed at IRIS or NASAs Planetary Data System (PDS). The data is generally affected by gaps and is thus separated into different sub-traces for many days. The number of gaps and their location in time can also be different for each component. For this study we heavily use the seismological python package ObsPy (*Beyreuther* et al., 2010a) for the reading, pre-processing and writing of the data.

Figure 3 displays the raw waveform of the V component, the corresponding spectrogram in power spectral density (PSD) and the wind data for three exemplary sols (338-340). Note the shared time axis in sols and local mean solar time (LMST), which is the local, dial time frame on Mars. The frequency is plotted up to the Nyquist frequency of 10 Hz (for 20 sps data). The raw data already reveal distinct features with periodic occurrence that are valid throughout the entire period of data acquisition. First, we can clearly distinguish between a period of high amplitude environmental noise throughout the martian day, ∼6:00-16:00 LMST, and a quieter period during the evening, from 17:00-23:00 LMST. Times from 23:00-6:00 LMST have an intermediate noise level. The high noise periods throughout the day are correlated with strong wind speeds of 5-17 m/s, whereas the during the quiet periods the wind does mostly not exceed 5 m/s. Secondly, we see some high energy narrow bands in the spectrogram, that slightly modulate in frequency throughout the sol

and are significantly less pronounced in the quiet times of the evening. These narrow band features are wind induced resonance modes of the lander, are labeled by their mean center frequency and will be discussed in more detail. We will further refer to them as lander modes. There is also a broader periodic signal centered around 2.4 Hz covering a wider range of frequencies between 2.2 and 2.7 Hz and is more pronounced during the quiet periods. We will refer to this signal as the 2.4 Hz mode and will establish, that it is fundamentally different than the other modes. The high amplitude spikes in the waveform that map as broadband signals into the spectrogram, covering all frequencies, are spurious signals, refered to as glitches, and will be discussed in detail in Section 4. Another prominent spurious signal is the so-called ticknoise, a distinct constant 1 Hz signal mapped as a narrow horizontal line in the spectrogram. It also features harmonics from 2 up to 9 Hz, with usually decreasing amplitude. The ticknoise, its origin and removal are discussed in details in Section 4.

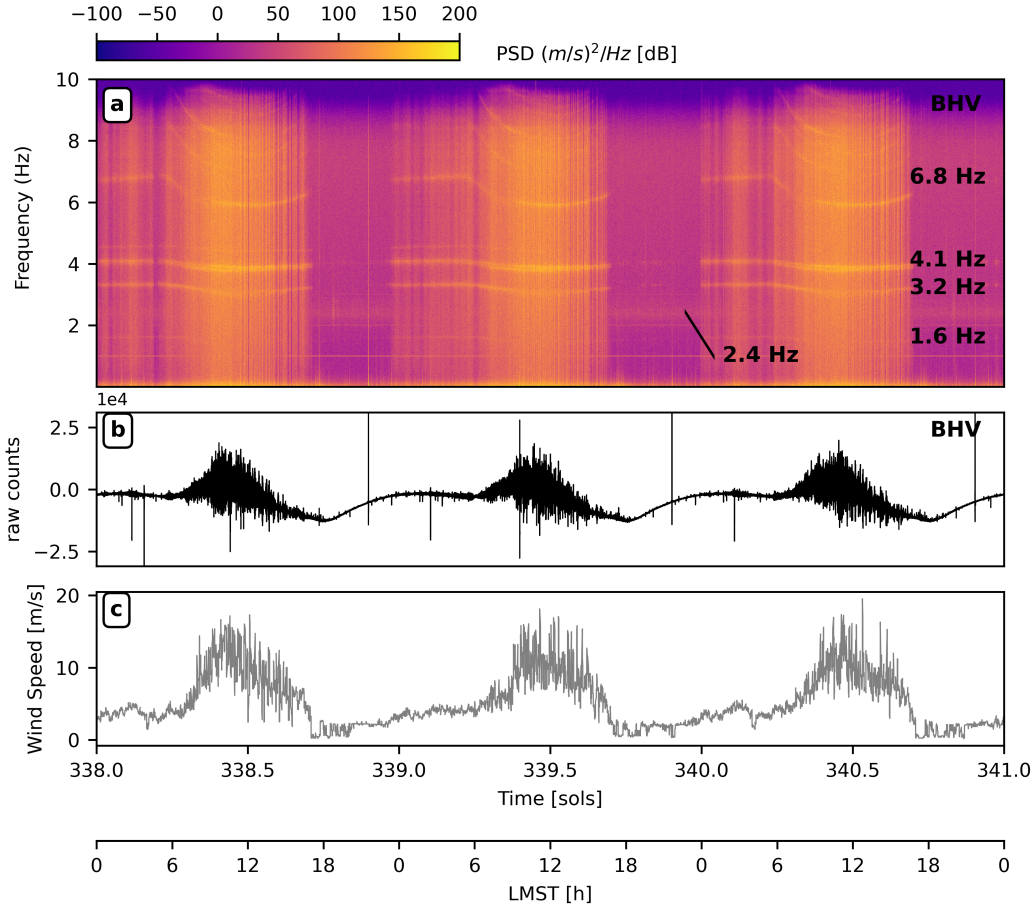

Figure 3: **(a)** Spectrogram in power spectral density and **(b)** waveform for the V-component of the raw data, as well as **(c)** the corresponding wind speed data, for three exemplary sols from sol 338 to sol 340. The main lander modes as well as the 2.4 Hz mode and labeled. The time axis is presented in sols and LMST.

3.1.1 Lander Modes

If we look in detail we can determine several lander modes in the spectrogram as linear features that slightly modulate in frequency and strongly modulate in amplitude over the period of a sol (Fig. 3). We can identify the main lander modes at ∼1.6, ∼3.2, ∼4.1 and ∼6.8 Hz, which is consistent with a detailed study of the modes by *Dahmen* et al. (2021). As mentioned before, we consider the 2.4 Hz mode as a different type of signal that does not belong into the category of the lander modes. Additionally, we observe several modes above 8 Hz, which significantly decrease in frequency during the day. All modes generally decrease in frequency during the day roughly until noon and increase again until reaching the quiet periods in the evening. The strong amplification of the modes during the day correlates with the time of the strongest winds and suggests, that they are generated by wind driven resonance of the lander, transferred into the subsurface. Further, the same modes were also observed in the early phase of the mission, when the SEIS instrument was measuring, while still being mounted on the deck (*Panning* et al., 2020). *Dahmen* et al. (2021) investigated the lander modes in detail and found a temperature dependence of their frequencies. As the temperature rises throughout the day the lander warms up and reduces its material stiffness, which consequently reduces the frequencies of the resonances (*Dahmen* et al., 2021). They further determined several additional, temporary modes at 2.7, 3.7, 5.2, 6.2 and 7.9 Hz, that occur only in specific periods of the acquisition time (e.g. 6.2 Hz between sols 258-298). The authors suggest, that these temporary modes are related to the position of the robotic arm.

3.1.2 The 2.4 Hz Mode

The 2.4 Hz mode is fundamentally different from the lander modes. Compared to the latter it comprises a much broader bandwidth and wider, smoothly decreasing flanks. Its mean center frequency is slightly shifted for each component and it does not consist of a single peak, but features multiple peaks (*Dahmen* et al., 2021). The mode is the strongest throughout the quiet night period and is masked by the high noise level during the day. *Dahmen* et al. (2021) studied the 2.4 Hz mode in detail and found that its amplitude slightly increases with increasing wind speed. However, its frequency, centered around 2.4 Hz is very stable. In contrary to the previously discussed wind induced lander modes, it was not observed while SEIS was still mounted on the lander deck (*Panning* et al., 2020). Interestingly, the mode is excited by high frequency marsquakes. Some marsquakes can only be identified due the amplification of the 2.4 Hz mode (*Driel* et al., 2021). Potential origins of the mode and its implication for AC studies are discussed in Section 7.

4 Pre-processing and Removal of Spurious Signals

4.1 Removal of Spurious Signals

The waveform for all three components (U,V,W) is generally contaminated by spurious signals (e.g. Fig. 3). In this section we will discuss the most prominent of these waveform perturbations and the attempt to remove them. Their removal is crucial for this study, as periodic signals or signals with periodic occurrence will contaminate the autocorrelation

with strong periodic energy that could be erroneously interpreted as arrivals from reflected phases.

4.1.1 Ticknoise

The ticknoise is an spurious signal with a periodicity of exactly 1 Hz, that can be observed as a peak in the spectra or a narrow horizontal line in the spectrogram (e.g. Fig. 3). It is produced by the electronic crosstalk of the temperature sensors within the SEIS instrument (*Ceylan* et al., 2020; *Zweifel* et al., 2021) and affects all three VBB components. It is present throughout the entire Martian sol but more pronounced within the quiet evening and night hours. It is strongest on the W-component and weakest on the U-component. The ticknoise can significantly contaminate the ACs with periodic oscillation of 1 s as shown by *Kim* et al. (2021) and has to be removed from the data. For its removal we use a method proposed by *Zweifel* et al. (2021), who studied the ticknoise in detail. Hereafter, we essentially cut the waveform into chunks with the length of 1 s and stack these data chunks to obtain a fairly well approximated waveform of the ticknoise. As recommended from the authors, we apply a first order highpass filter (0.1 Hz) to the data prior to the stacking procedure, to improve the estimation of the noise waveform. To mitigate the disturbance of the stack by glitches or very noisy data windows, data chunks that exceed a threshold in amplitude variance are rejected from the stack, providing a more accurate retrieval of the ticknoise waveform. We tested the variance threshold experimentally and chose a value of 10^4, as it produced the best results for us.
Figure 4 shows the ticknoise waveform for the three components derived from the described method for an exemplary day in UTC time. Note that the waveform varies between the different components. Once the waveform for the ticknoise is extracted it can be simply subtracted from the raw waveform to obtain the "deticked" data. This method has the advantage of retaining the remaining energy in around the 1 Hz which is lost in case of applying a notch filter. Figure 4 shows the comparison between the raw and the deticked data. Note that the strong coherent energy at 1 Hz that is present throughout the entire sol disappears on all components. However, we realized that this approach works only for parts of the data as we still find significant residual peaks of the ticknoise, despite of the attempted removal. Thus, we transformed the data to the frequency domain and set the residual peaks to a mean of the surrounding values as further proposed by *Zweifel* et al. (2021), while we preserved the phase. The data is then transformed back into the time domain and we continue the processing sequence.

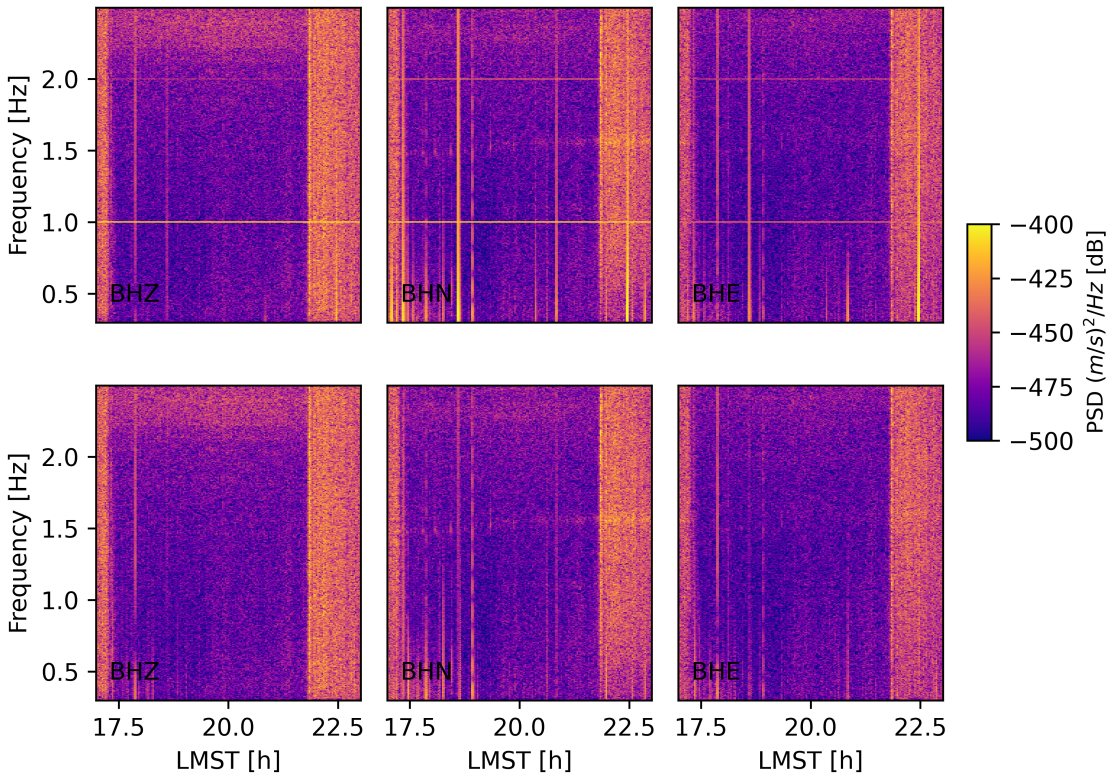

Figure 4: Spectrograms (PSD) of the raw (top row) and deticked (bottom row) data of the quiet evening period, 17:00-23:00 LMST, of the exemplary sol 210, for all three components. The method used for the noise removal is discussed in the text.

4.1.2 Glitches

Glitches are one-sided broad band high amplitude pulses within the waveform that last up to ∼25 s and can contaminate all components of the VBB instrument as revealed by a detailed study of *Scholz* et al. (2020). The authors found that the glitches usually consist of low frequency main lobe and a spike-like high frequency precursor signal at the onset of the main pulse. *Scholz* et al. (2020) relate the glitches to the strong temperature gradients that are experienced by the instrument on the Martian surface. The temperature difference between times during the martian day and the night can reach up to 100 K (*Compaire* et al., 2021), introducing a challenge for the design of the instrument. The SEIS instrument is covered by thermal shield, protecting the electronics from being damage by extreme temperatures. However, the resulting temperature gradients within the instrument can still reach up to 15 K (*Scholz* et al., 2020), which is four magnitudes higher than temperature gradients conventional seismometers on earth are exposed to.
Scholz et al. (2020) further proposed the glitch generation mechanism as an instantaneous deformation of the material within the instrument, caused by thermal expansion of the material. The instantaneous deformation translates to a sudden step in the acceleration. The spiky precursor signal thereby corresponds to a step function in the displacement. The convolution of these particular sequences with the instrument response then yields

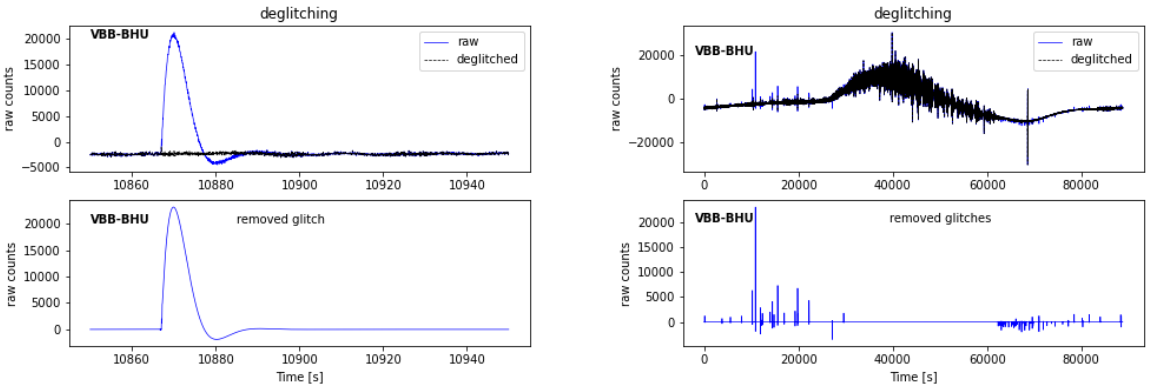

(a) (b)

Figure 5: **(a)** Waveform for an exemplary glitch detected and removed from the U-component during sol 235. **(b)** Raw (top) and deglitched waveform of the U-component for the exemplary sol 235. The method used for the glitch removal is discussed in the text.

the particular waveform of the glitches. Glitches can map directly into the ACs, in particular in the later lags depending on their separation in time as demonstrated by *Kim* et al. (2021). Thus it is crucial to remove them from the data before performing any AC analysis. Their generally broadband spectral content impede a straight forward removal by frequency filtering. *Scholz* et al. (2020) further provide a method using the described generation properties, designing a template fitting algorithm. First they compute the time derivative of the dataset, that is deconvolved the with the instrument impulse response, to obtain spikes for the glitches. Secondly, for the detected spikes, the waveforms of the glitches are modelled and compared to the raw waveform. The fit is defined as sufficient, when the root-mean-squared (RMS) amplitude is reduced by a certain threshold or more, by subtraction the modelled glitch from the real data. When the RMS amplitude is not reduced sufficiently, the suspected glitch is not removed from the data. Figure 5 illustrates the raw data before and after the performance of the glitch removal algorithm from *Scholz* et al. (2020). We note, that many glitches are removed, but many potential glitches remain in the data as well. However, we generally observe, that this method is limited to the quieter periods of the sol, as no glitches could be detected and removed during the noisy period of the sol. Nevertheless, as we confine our data selection for the ambient noise analysis to the quieter evening periods anyways, this is not a severe limitation for our study.

4.2 Preprocessing

Once the ticknoise is removed from the raw data and the data is deglitched, we remove the instrument impulse response and convert the raw counts of the instrument into the physical units of the ground motion. Here we chose to work with particle velocity as the physical unit of our amplitude. The procedure of the instrument response removal is depicted in Figure S8 in the supplements. After the instrument response is successfully removed, we merge the different sub-traces with gaps in between for each component and interpolat the gaps in between. The interpolation avoids large discontinuities in the data,

that may introduce artefacts at further processing steps, like the application of a bandpass filter. All start and end times of the gaps are archived, such that the data containing gaps can be rejected at any point later on.
Thereafter, we rotate the axis from the oblique orientations U,V,W to the geographical orientations Z,N,E. The axis orientations, as well as the instrument impulse response, were obtained from the metadata for the VBB instrument. Finally, we convert the data from UTC day times to the actual Martian sols, using a conversion method provided by Dr. Savas Ceylan from the MQS, and remove the trend and the mean from the data.

4.3 Supression of Lander Modes

In Section 3 we have already described the wind induced lander modes. As the modes are particularly amplified from the morning until the afternoon of the Martian sol, when the wind is strongest, we restrict our data selection to the quiet early evening and night period from 17:00 to 23:00 LMST. This is further justified, as we can not detect and remove the glitches during this period of the sol. Figure 6 illustrates the spectrograms and the corresponding average spectras for the quiet evening period, for all three components and the entire data set. From the average amplitude spectras we can visually determine the mean frequencies of the lander modes as well as suitable cutoff frequencies for each particular mode and each component. The significantly increasing noise level from sol ∼520 onwards marks the beginning of the Martian Winter (*Spiga* et al., 2021) with higher wind speeds (*Schimmel* et al., 2021). Note that the 2.4 Hz mode is significantly stronger on the vertical component than on the horizontal ones, which was also confirmed by polarization analysis (e.g. *Hobiger* et al., 2021; *Dahmen* et al., 2021).
We apply a fifth-order zerophase butterworth bandpass filter between 0.3-8.5 Hz and several bandstop filters to the data to suppress the lander modes that are present even in the quiet period of the sol. As different components are affected by different modes or as the particular frequencies of the mode vary for different components, we apply different filters to each component. An overview of all the determined modes and the applied filters to mitigate them is given in Table 1. We note that, fortunately, our main target for this study, the vertical component, is only affected by one strong lander mode at 4.1 Hz, of which the band is also significantly narrower compared to the horizontal components (Fig. 6).

Table 1: List of lander modes and the applied filters for their suppression. The numbers represent the frequencies in Hz, where the frequency range describes the corner frequencies of the applied bandstop filters. The lander modes are named after their mean center frequency (e.g. 1.6 is a lander mode with a mean center frequency of 1.6 Hz)

Lander Mode / Component	Z	N	E
1.6	-	1.48-1.61	-
3.2	-	3.12-3.40	3.20-3.38
4.1	3.90-4.20	3.83-4.34	3.81-4.34
6.8	-	6.62-6.85	6.54-6.86

Figure 7 shows the same spectrograms and amplitude spectras for the data after applying the described filtering. The lander modes are strongly suppressed by the bandstop filters.

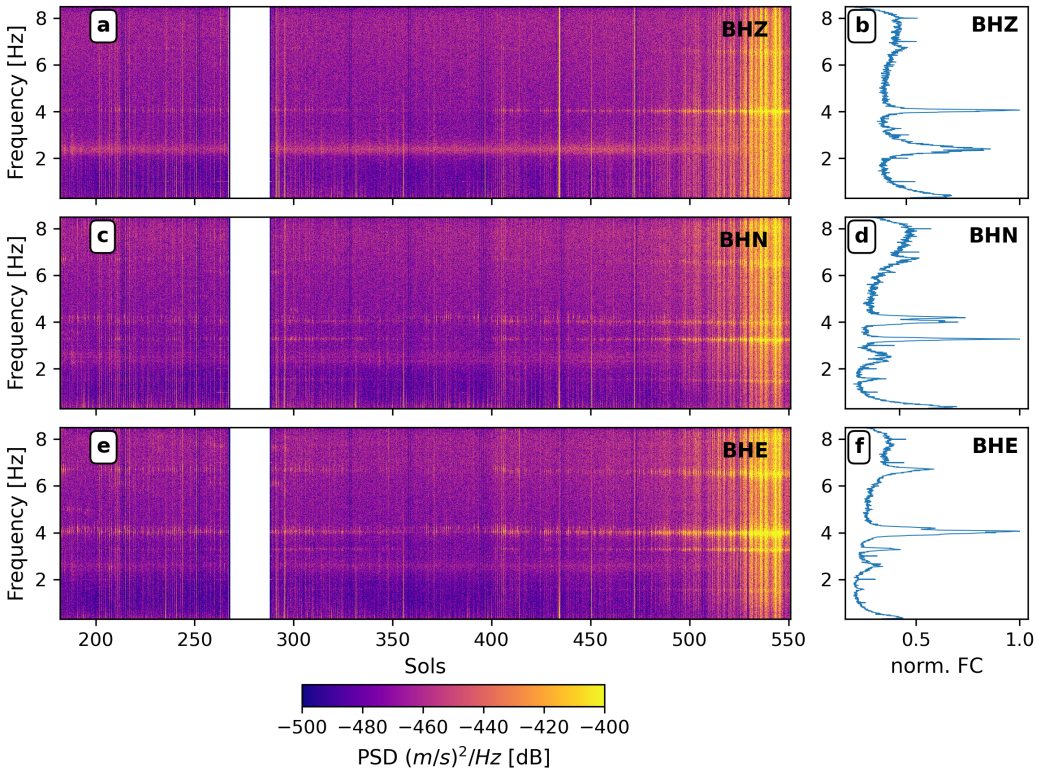

Figure 6: **(a,c,e)** Spectrograms (PSD) and **(b,d,f)** mean spectras for the processed data for all three components, bandpass filtered from 0.3-8.5 Hz. Only data of the Martian evening between 17:00-23:00 LMST is considered here. The spectrograms are computed with windows of 30 min lengths and 60 % overlap. The mean spectras are normalized by the maximum for each sol; the resulting amplitude is labeled as normalized Fourier coefficients (FC). The bold labels denote the IDs of the data channels.

Note the strong gap in the frequency band that is necessary to suppress the 4.1 Hz mode which frequencies vary over the period of the data acquisition and thus require a broad bandstop filter compared to the other modes.

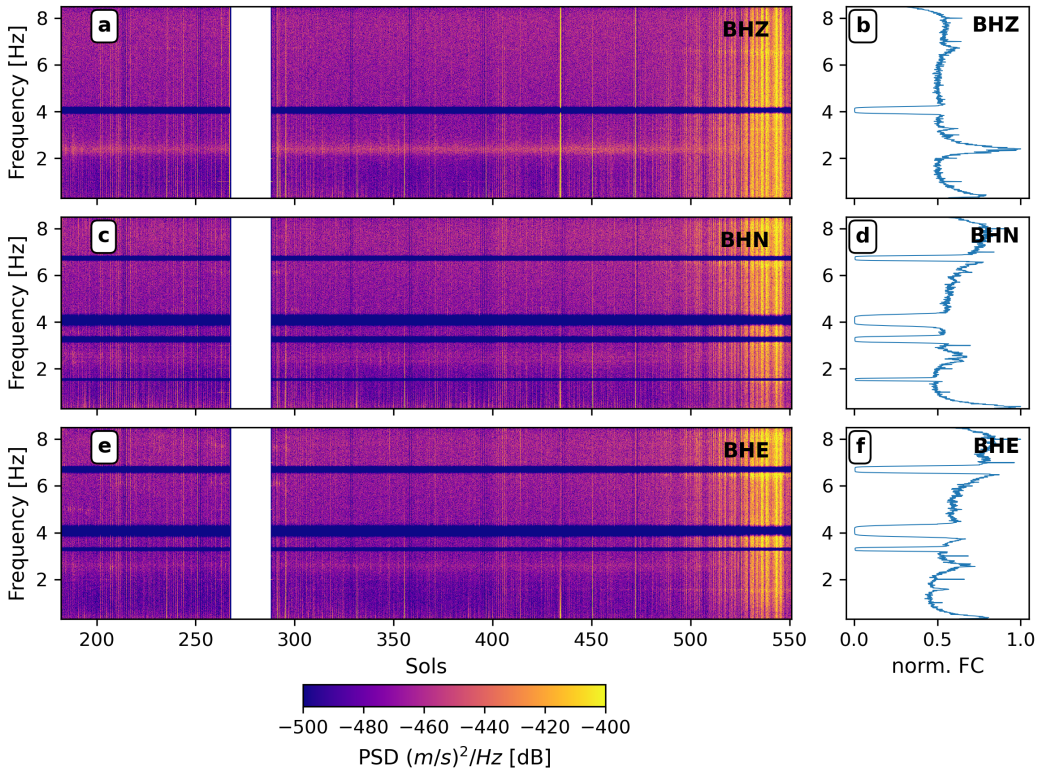

Figure 7: Same as Figure 6 but after applying the set bandstop filters to suppress the lander modes.

4.4 Amplitude Balancing

In order to further attenuate the effects of transient signals with large amplitude (e.g. glitches that were not removed by the deglitching algorithm), we apply amplitude balancing in form of a moving window normalization as recommended as a pre-processing step for ambient noise correlation methods by *Bensen* et al. (2007). This amplitude normalization essentially breaks down to a moving average. For each sample of the time series a weight is assigned as:

$$w_n = \frac{1}{2\ N+1} \sum_{j=n-N}^{n+N} x_j \tag{1}$$

and the normalized trace is given by $x_{n,norm} = x_n w_n$. The crucial parameter for this method is the window length for the weight assignment N. Here, we use as further recommended by *Bensen* et al. (2007) half of the period of lower edge of the applied bandpass filter. Using a lower corner frequency of 0.3 Hz we thus obtain a window length of $0.5\frac{1}{0.3} = 1.67s$ which corresponds to 33 samples considering the sampling rate of 20 sps. In order to prevent the rise of artefacts, the interpolated gaps in the data are muted after the amplitude balancing. Another method proposed by *Bensen* et al. (2007) and used in other AC studies on the SEIS data (e.g. *Compaire* et al., 2021) is one-bit normalization, where each sample is reduced to either 1 or -1 accordingly to the sign of its amplitude. As

this method preserves no amplitude information except for the sign, we favor the moving average normalization.

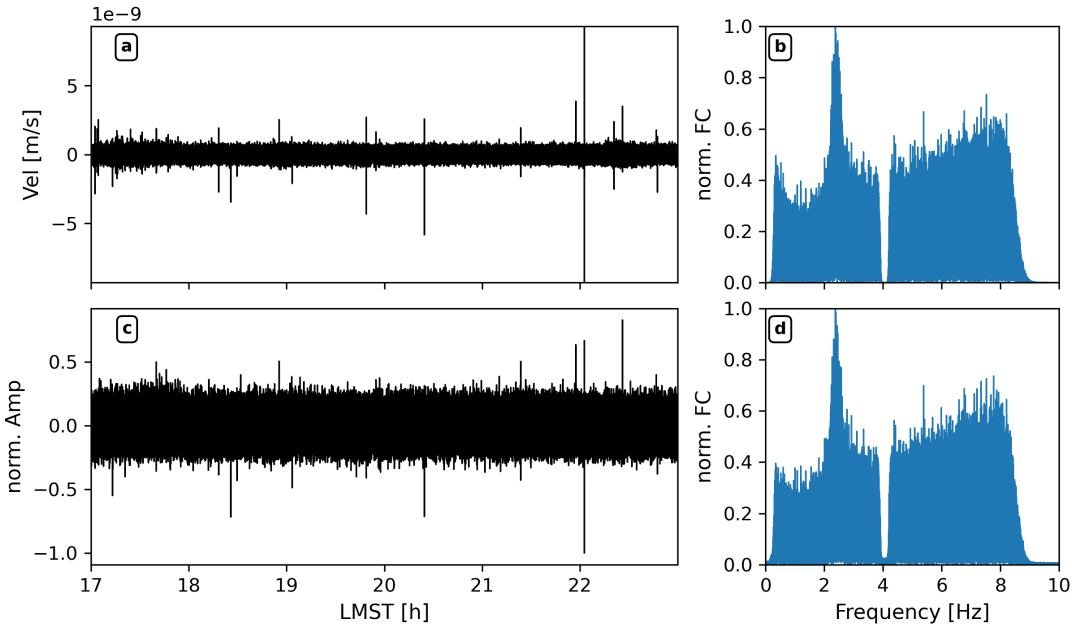

Figure 8: Processed trace of the vertical component and the corresponding spectra **(a,b)** without and **(c,d)** with moving average amplitude balancing after *Bensen* et al. (2007) for the evening hours of the exemplary sol 339. The traces are bandpass filtered from 0.3-8.5 Hz and filtered with the previously described bandstop.

The effect of the sliding window normalization on the waveform and the corresponding amplitude spectrum is illustrated in Figure 8 for the vertical component of the exemplary sol 339. Remaining transient signals in the data (e.g. spikes) are attenuated, while the spectrum remains unchanged.

5 Computation and Evaluation of Autocorrelation

5.1 Ambient Noise ACs

In order to compute the ambient noise ACs we first cut the data into windows of ∼6 min lengths, that overlap 60 s, resulting in 295 data windows per sol, from which 75 fall in the quiet evening periods that we use in this study. We chose a window length of 6 min for the ACs as a tradeoff, as longer windows generally provide a stronger enhancement of periodic signals, but short windows enable more flexibility in rejecting partly contaminated data. Hereupon, we taper each window with a Tukey window (*Harris*, 1978) to mitigate edge effects and compute the ACs for maximum lag times of 60 s. Additionally, we partition the wind data in similar fashion and compute a mean wind speed and a corresponding standard deviation for each data window. We then evaluate each particular window in terms of the assigned wind attributes and either use its AC for stacking or reject it in case it exceeds the defined thresholds of 5 m/s and 1.5 m/s standard deviation. As there

are some residuals of the lander modes, glitches and ticknoise, some AC windows show strong periodic oscillations, that contaminate the stack. In order to prevent the inclusion of these contaminated ACs we apply an amplitude threshold for lags later than 10 s. ACs, of which lag times, greater than 10 s, exceed this amplitude threshold are rejected from the stack. The amplitude threshold is determined experimentally and is set to 25 % of the zero lag amplitude. An exemplary AC gather containing the rejected ACs is illustrated in the supplements (Fig. S7). We relate the observed strong oscillations to the residuals of the spurious signals.

5.2 Marsquake ACs

In addition to the ambient noise ACs (AACs) we compute the ACs for a selection of marsquake events and their corresponding coda (MACs). For this purpose we use the assigned picks for start and end times for each event from the MQS (*Clinton* et al., 2021; *InSight Marsquake Service*, 2021) and extract the corresponding chunk of data from our processed dataset. We then apply the same bandstop filters to the data as for the AAC computation. *Lognonné* et al. (2020) found that the wavefield of the marsquakes becomes rather diffusive right after the onset. Hence, we use the entire marsquake waveform for the AC computation. From ∼490 detected marsquakes (*InSight Marsquake Service*, 2021) we use 50 high frequency events (HFs), 176 2.4 Hz events and 24 very high frequency events (VFs) resulting in a total of 250 events. We only use marsquakes that have quality label of A-C (scale A-D, where A equals high and D equals low quality) assigned by the MQS. A quick overview of the marsquakes, that are used in our study, and their frequency content is listed in Table 2. Since we are only using events from the three HF families containing frequencies between 1-10 Hz we bandpass filter the events between 1-8 Hz.

Table 2: Overview of marsquakes used for the MAC computation. The frequencies are in Hz.

Marsquake type	Frequency content	Number of events	N quality 'B'
HFs	1-10	50	32
2.4 Hz events	mainly 2.4	167	37
VFs	HFs but polarized in N,E	24	11

5.3 Phase Weighted Nonlinear Stacking

Beside the ordinary linear stacking of ACs we also perform a phase weighted nonlinear stacking (PWS), as proposed by *Schimmel* and *Paulssen* (1997). Phase weighted stacking enhances coherent signals and is thus a common technique in AC or receiver function studies, where weak arrivals are present, but hidden within multiple noisy traces. As only the phase is used for the weighting, the method is amplitude unbiased, and hence is advantageous for data that is affected by incoherent noise, which is attenuated.
First, we transform our real trace $s(t)$ to a complex trace $S(t)$ using the Hilbert transform $H(t)$ as:

$$S(t) = s(t) + iH(s(t)) = A(t)exp(i\phi(t)) \tag{2}$$

Where i is the imaginary unit, and $A(t)$ and $\phi(t)$ are the time-depending amplitude and phase, respectively. The stack of traces is maximal if the phases of corresponding samples are equal. By normalizing the dataset of N traces sample by sample with its absolute, the amplitude independent phase stack $c(t)$ is obtained as:

$$c(t) = \frac{1}{N} \sum_{j=1}^{N} exp(i\phi_j(t)) \tag{3}$$

The amplitude of the phase stack results thereby in values between zero and one, representing inverse coherent and perfectly coherent signals, respectively. Finally, the PWS $g(t)$ is obtained multiplying the phase stack as a weight with the linear stack (*Schimmel* and *Paulssen*, 1997):

$$g(t) = \frac{1}{N} \sum_{j=1}^{N} s_j(t) [\frac{1}{N} \sum_{k=1}^{N} exp(i\phi_k(t))]^v \tag{4}$$

where v is a meta parameter controlling the sharpness of transition between phase similarity and dissimilarity (*Schimmel* and *Paulssen*, 1997). Note that setting $v = 0$ retrieves the ordinary linear stack. Here in this study we use a squared phase weight ($v = 2$).
We tested computing the PWS in three different approaches:

1. We compute the AC for each data window, attribute filter the results and stack all ACs for each sol linearly. Afterwards, we compute the PWS of all the linear stacks to obtain the mean of the entire data set.

2. After the attribute filtering we compute a PWS for the ACs of each sol. The resulting ACs (one per sol) are then again stacked with a PWS.

3. Finally, we compute a PWS directly from all ACs passing the attribute filtering.

The comparison of the results of these three different approaches is presented in Figure S2 in the supplements. All PWS approaches show the similar arrivals and significantly improve the stack compared to the ordinary linear stack. However, we note that first method is less noisy than the other two and we decide to use this approach for our further analysis. We also observe from the spectras, that the first method does not enhance the residual of the 4.1 Hz lander mode energy as much as the other methods and does not boost high frequency noise >8 Hz.

6 Results from Autocorrelation

In this section we present the results for the AC computation and subdivide them into AACs and MACs. For each method and component we show the AC gather represented by the mean ACs for each sol, the corresponding linear stack, the PWS and the mean amplitude spectra for all the ACs. We pick the arrival times on the PWS as they are usually shaper and less ambiguous than the linear stack.

6.1 Ambient Noise ACs

Figures 9-11 show the results of the AACs with applied attribute filtering for all three components. For a comparison, the result for the AC computation for the vertical component without any attribute filtering is demonstrated in the supplements in Figure S1. The gather looks very similar to the gather in Figure 9 but contains several traces, that feature high amplitude oscillations, which are removed by the attribute filtering. The ACs that are removed due to exceeding the high amplitude threshold are displayed in Figure S7 in the supplements. Further, we decided not to use data from sols before sol 180 as there are many gaps in the 20 sps VBB data as the acquisition configuration was switched back and forth between 10 and 20 sps. Further we do not use data from sols beyond sol 520, as the data gets significantly more noisy even in the quite night period which is due to the seasonal weather change, reaching Martian winter (e.g Figs 6; & *Spiga* et al., 2021). The ACs computed with the entire dataset (from sols 83-740) not rejecting any data due to the wind data are illustrated in Figure S6 in the supplements. Note the gap within the dataset from sol 266 to sol 287 due to the solar conjunction (*Ceylan* et al., 2020), where the sun is located in between Earth and Mars and the magnetic field disturbs any communication between the mars orbiger and Earth (*NASA*, 2021a).

First we analyze the vertical component, our main target in this study (Fig. 9). Note that the PWS enhances coherent signals and yields a significantly improved stack displaying sharper arrivals compared to the ordinary linear stack. Here, 5 % of the ACs are rejected by the attribute filtering. For the vertical component we observe main arrivals at ∼10.8, ∼12.7, ∼20.8, ∼30 s. There may be another arrival around 6 s but the energy might also be related to the leak of the zero lag. In the AC gather we can observe the arrivals, in particular the 10.8, 12.7 and 20.8 s arrivals as consistent features through the entire period of the considered dataset. As they are still present after the attribute filtering, we can exclude wind noise or the mentioned strong oscillating produced by spurious signals as their origin (compare Figs 9 & S1).

The results of the north and east components are more difficult to analyze than for the vertical component in the band from 0.3-8.5 Hz, as they are dominated by high frequencies and not by the 2.4 Hz mode like the vertical component. Without suppressing the higher frequencies, we can not identify any clear arrivals. We thus use a narrower bandpass filter from 0.3-3.0 Hz to analyze the horizontal components. Analyzing different components with different band widths is not ideal but necessary in this case. We also note that with this approach, the spectras of all three components are dominated by the 2.4+Hz mode. The AACs for the horizontal components using the broader band from 0.3-8.5 Hz are presented in Figures S4 & S5. Conversely, AACs for the vertical component filtered between 0.3-3.0 Hz are shown in Figure S3.

Using the narrower band from 0.3-8.5 Hz we can identify potential arrivals at ∼12.1, ∼16.5 and ∼22.6 s for the north and at ∼12.4 and ∼17 s for the east component. On both components we relate the significant amount of energy around ∼9 s to the leak of the zero lag. Within the narrow band for the north and east components only 2 and 3 % of the data were rejected, whereas for the broader bandwidth, 15 % and 25 % were by the attribute filtering, respectively. The larger amount of rejected data is likely due to the residuals of the lander modes that are still present in the frequencies above 3 Hz on the horizontal components.

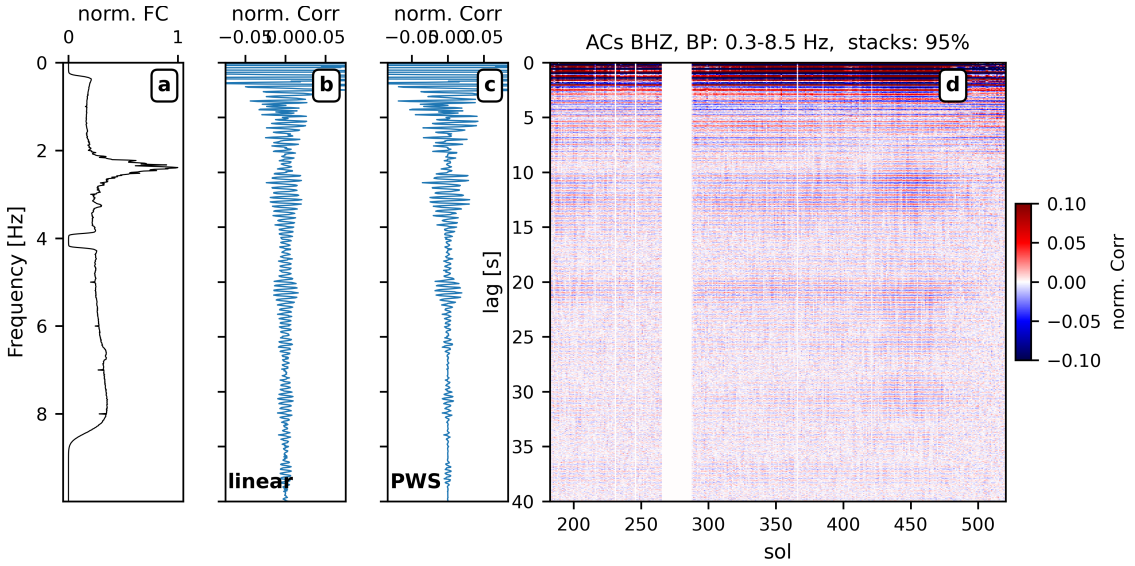

Figure 9: **(a)** Amplitude spectra, **(b)** ordinary linear stack, **(c)** PWS and **(d)** gather for the AACs of the vertical component. The amplitude spectra is computed as a mean from all ACs and normalized. The gather shows the linear AC stacks for each sol. Around 5% of the considered data windows are rejected by the attribute filtering. Both the AC gather as well as the stacks are normalized by their maximum at the zero lag and clipped for visualization.

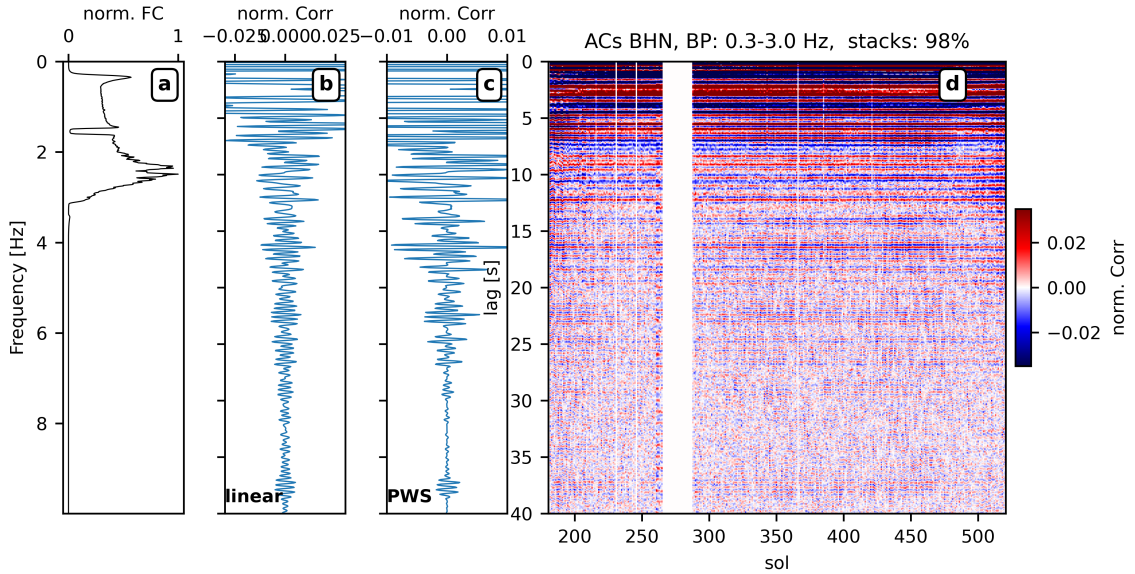

Figure 10: Same as Figure 9 but for the north component and in the narrower band from 0.3-3 Hz. Only 2 % of the data is rejected by the attribute filtering.

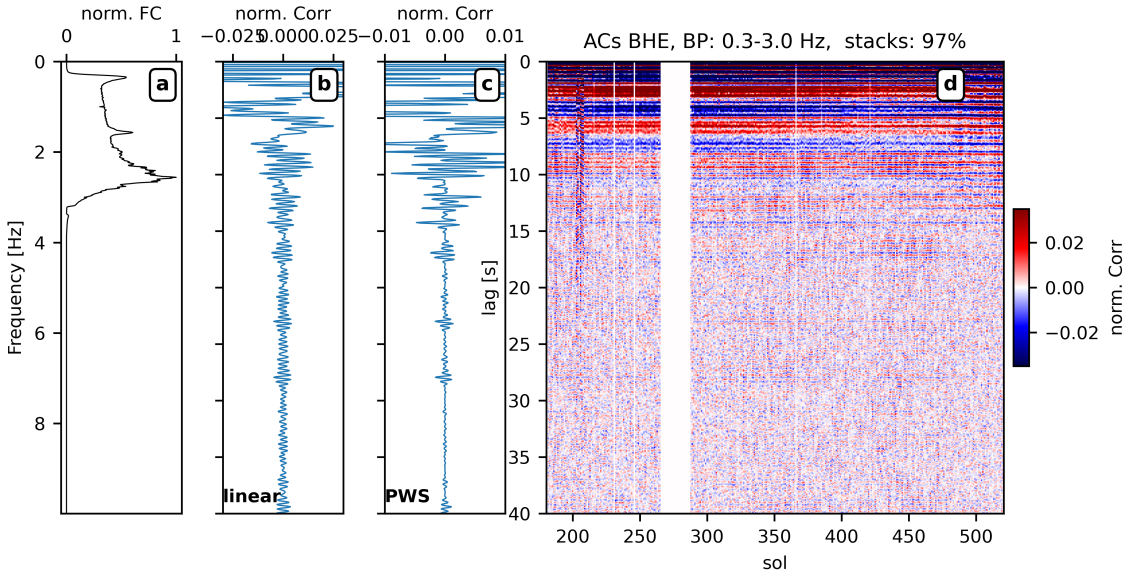

Figure 11: Same as Figure 9 but for the east component and in the narrower band from 0.3-3 Hz. Only 3 % of the data is rejected by the attribute filtering.

6.2 Marsquake ACs

Figures 12-14 show the results for the MACs. We illustrate them in the same way as the AACs before. The processing steps and the quake selection procedure is described in Section 5.2. For the vertical component no arrivals can be observed consistently throughout the AC gather. From the stacks we can deduce arrivals at lag times ∼5.8, ∼7.0, ∼10.5, ∼12.8 and ∼21 s, that are in particular visible on the PWS (Fig. 12). Moreover, we observe, that the mean spectra is entirely dominated by the 2.4 Hz mode, which is consistent with its excitement by the HFs, in particular the 2.4 Hz events. For the north component we can observe two main arrivals at ∼16.5 and ∼22.4 s, again in particular identifiable on the PWS. Another arrival could be present at ∼9 s, but is not obvious. Conversely to the vertical and north components, the east component is quite difficult to interpret. There may be potential arrivals at ∼10 and ∼13.3 s but they are rather ambiguous. In the mean spectras we can observe lander mode residuals at 6.8 Hz for the north and at 3.3, 4.1 and 6.8 Hz on the east component. However, the main energy is located in the 2.4 Hz band for the horizontal components as well.

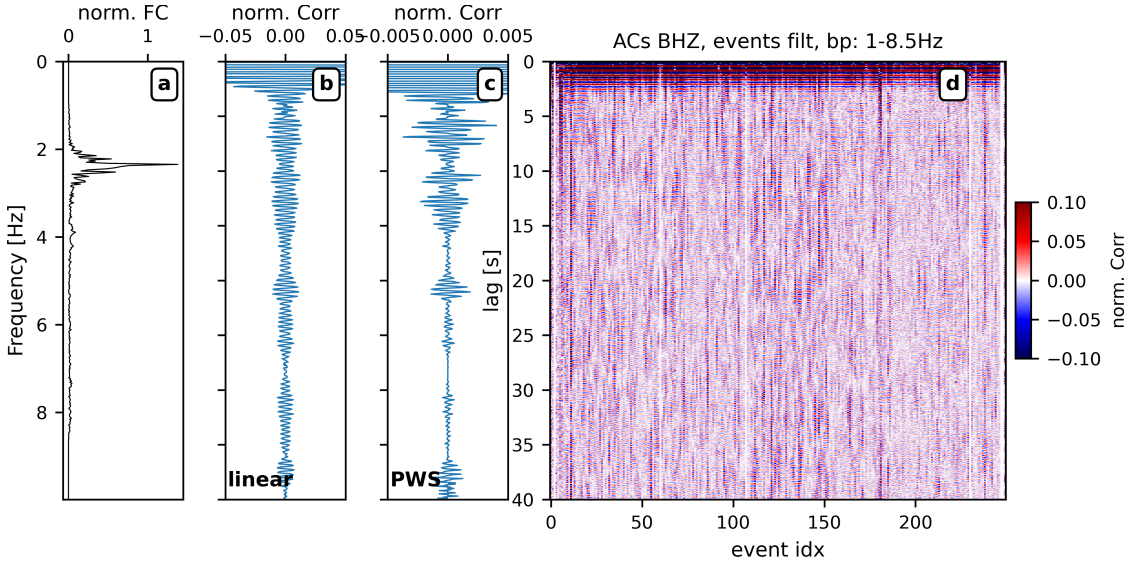

Figure 12: **(a)** Amplitude spectra, **(b)** ordinary linear stack, **(c)** PWS and **(d)** gather for the MACs of the vertical component. The amplitude spectra is computed from the linear stack and normalized. The gather shows the AC for each marsquake. Both the AC gather as well as the stacks are normalized by their maximum at the zero lag and clipped for visualization.

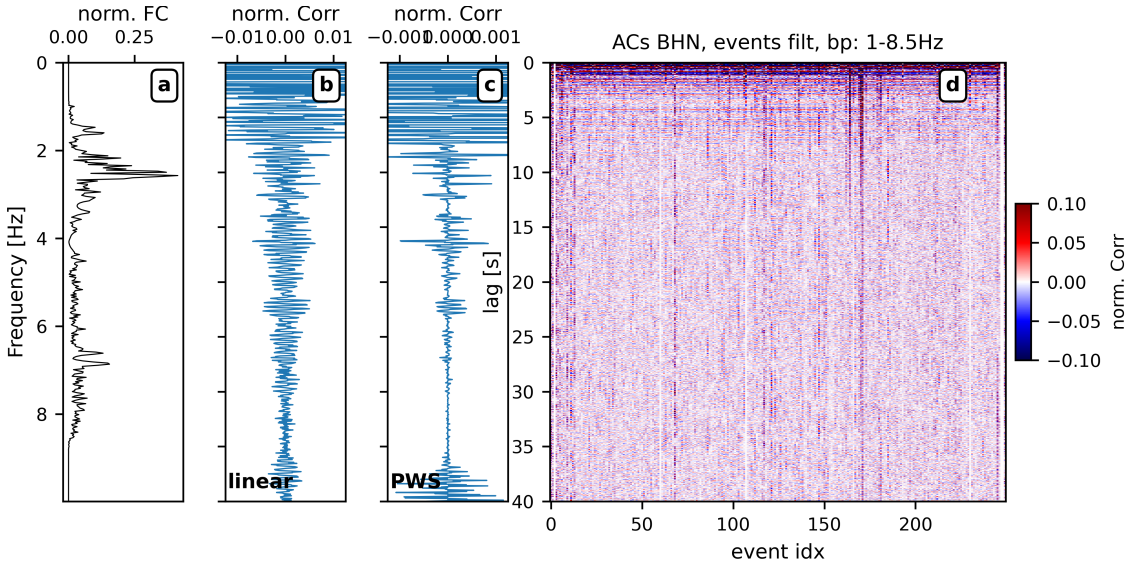

Figure 13: Same as Figure 12 but for the north component.

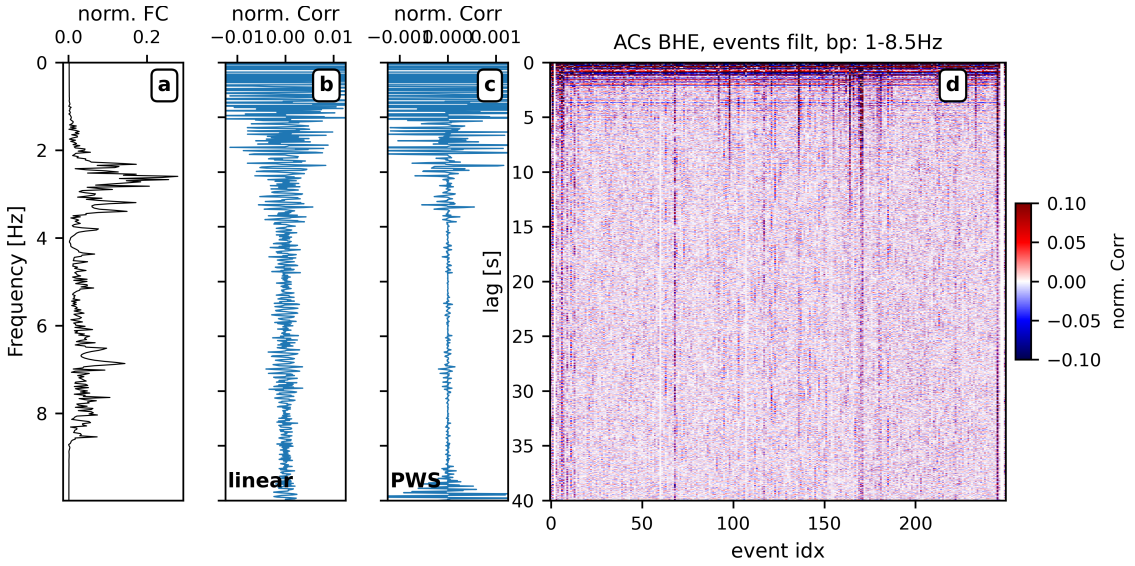

Figure 14: Same as Figure 12 but for the east component.

6.3 Comparison AACs & MACs

Figure 15 depicts the comparison between the stacks of the AACs and MACs for all three components. Here, we focus on lags between 5 and 30 s. As all stacks are clipped differently for better visualization, we omit any amplitude scale. In general, we find a very good agreement between the arrivals obtained by the two methods. For the vertical component the arrivals ∼10.8, ∼12.7 and ∼20.8 s agree on both methods. The distinction between the two arrivals at 10.8 and 12.7 s is significantly more clear in the PWS of the MACs. It is not obvious in the AACs, in particular in the linear stack. On the north component the two arrivals at 16.5 and 22.6 s agree very well, whereas the arrival at 12.1 s is identifiable but less obvious in the MACs. The east component is again the most difficult to assess. We picked arrivals at 12.4 and 17.0 s on the AACs, which are not

visible in the MACs. Instead, we observe an arrival at roughly 13.8 s in the PWS of the MACs. Both horizontal components show again a large amount of energy at lag times of ∼9 s, consistent over both methods, which is however very close to the zero lag and thus is excluded from the analysis.

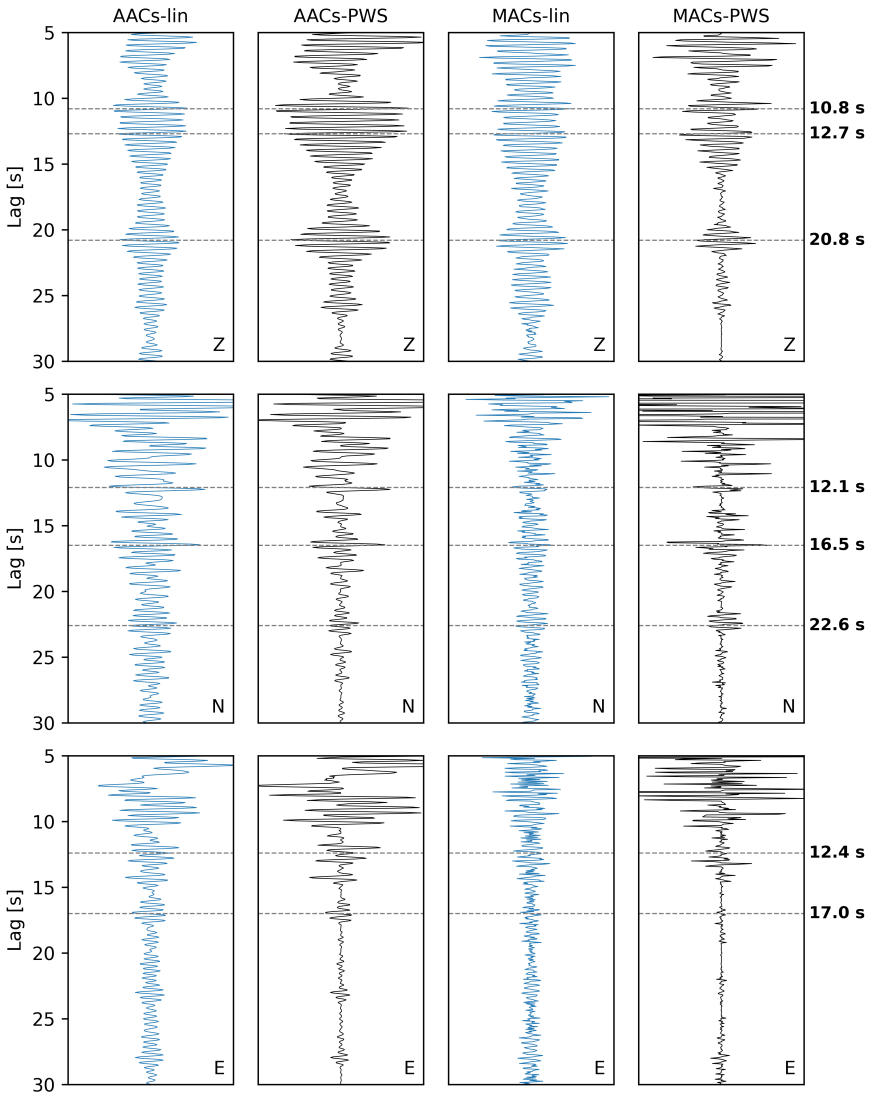

Figure 15: Compilation of the AC stacks for both methods, AACs and MACs, for all three components. The linear stacks and the PWS are plotted in blue and black, respectively. Each row represents the stacks for one component which is denoted in the lower right corner. The left two column correspond to stacks from the AACs whereas the two right columns are from MACs. The main picked lag times for the inferred arrivals is shown as horizontal dashed lines.

6.4 Removing the 2.4 Hz Mode

Since the ACs for both methods are mostly based on the 2.4 Hz mode, we tested the influence on the ACs for removing the 2.4 Hz energy with a broad bandstop filter between 2.1-2.65 Hz. The broad bandstop is necessary due to the wide flanks of the mode. Figure 16 shows the resulting vertical AACs and the corresponding spectra. The main arrivals that characterized the ACs including the 2.4 Hz mode, namely at ∼12.4 and ∼21 s can no longer be identified (compare Figs. 9 & 16). There is some energy left at lag times of ∼11 s, only visible on the PWS. However, it is dubious and should be interpreted with caution.

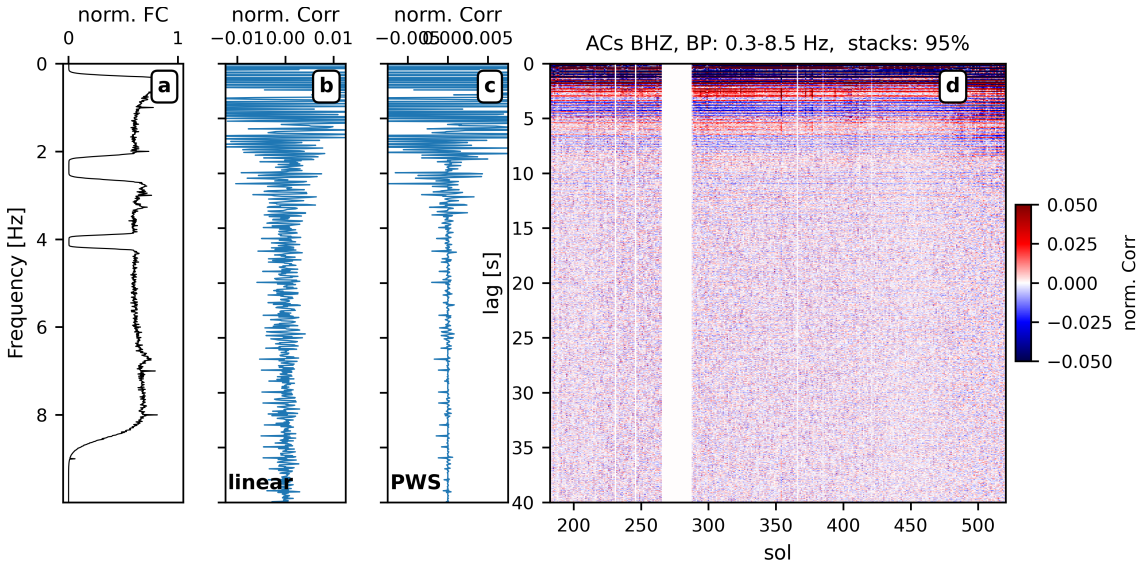

Figure 16: Same as Figure 9 but now with a 2.2-2.65 Hz bandstop filter applied on the 2.4 Hz mode.

7 Discussion

7.1 Influence of Spurious Signals and Lander Modes

7.1.1 Lander Modes

The lander modes and their generation is described in Section 3. We also described our filtering approach to attenuate those modes in Section 4. However, we observed from the amplitude spectras of the ACs, that the modes are not completely removed by our filtering approach. Consequently, as the AC is essentially a multiplication of the spectra with itself, the residual modes amplify in the autocorrelograms. In particular the horizontal components are affected by the residual modes (e.g. Figs. S4a & S5a). Their variance in time of both center frequency and bandwidth, which is related to the time dependence of wind and temperature (*Clinton* et al., 2021; *Dahmen* et al., 2021), impedes their removal with simple, constant bandstop filters. For better results in removing these modes a more flexible, time variant approach of estimating their properties needs to be applied. *Dahmen* et al. (2021) recently showed an approach of automated tracking of

the lander modes which may have potential to better suppress them in future studies. However, we note that our main focus in estimating the subsurface reflectivity is the vertical component which is revealing distinct arrivals in the ACs at ∼6, ∼11 & ∼21 s. These arrivals are also present in the band that is bandpass filtered between 0.3 and 3.0 Hz (Fig. **??** in supplements), which does not contain any lander modes. Thus, we can rule out the lander modes as a source of theses arrivals in our ACs. Further, *Kim* et al. (2021) showed that the main energy of of the lander modes is confined to the early lags in the ACs.

7.1.2 Remaining Glitches and Ticknoise

A lot of care is taken to remove the broadband glitches and the ticknoise from the data as described in Section 4.1. Despite of these efforts residuals of both of these artefacts remain in the data contaminating the ACs.

Glitches: As we can observe from the waveform (Fig. 5) and from the spectrograms (Fig. 6), after the deglitching there still remain some glitches in the data. *Compaire* et al. (2021) used the same deglitching algorithm from *Scholz* et al. (2020) and found, that for many glitches the high frequency precursor is not removed. The authors also studied the timing in between the glitches. They revealed, that the minimum and average time separating consecutive glitches is ∼30 and ∼200 s, respectively. Considering these time separations the remaining glitches should not map significantly into the ACs, in particular not for lag times below 30 s. Moreover, the moving average amplitude balancing that we apply to the data mitigates any remaining transient signals. Thus, we can rule out the interference of residual glitches as the source of our arrivals in the ACs, in particular the early ones (e.g. at ∼11, ∼12.5 and 21 s on the vertical component).

Ticknoise: the waveform of the ticknoise is obtained by stacking consecutive 1 s data windows, separately for each raw data file which corresponds to one day of UTC time. However, for some days its waveform may not be completely constant throughout the entire day. As the waveform that is estimated and subtracted is constant for each day, this approach results in a residual of the ticknoise and its harmonics for days where the ticknoise waveform is not constant. Secondly, days that are noisy hinder a precise estimation of the ticknoise waveform which also results in a residual after its removal. In fact, due to the significantly increasing noise level, even in the quiet periods of the sol, from sol ∼550 onwards the estimation of the ticknoise becomes more difficult (see Fig. 8 in *Kim* et al., 2021). This further justifies limiting our study to data not beyond sol ∼550. Despite of the attempted removal a residual of the ticknoise can still be observed in the spectra of the processed data (e.g Fig. 6, interestingly, mostly on its harmonics. However, we do not see a strong imprint of the ticknoise in the ACs. We would expect strong oscillation with a periodicity of 1 s and its harmonics in the ACs, which is not the case. Potentially, the implemented amplitude threshold for lags >10 s may additionally filter out AC windows which contain a still strong ticknoise residual.

7.2 The 2.4 Hz Resonance

As depicted by the spectrograms and the mean spectras (e.g. Fig. 6), the main energy on the vertical component during the quiet night period on Mars is found in the band of the 2.4 Hz mode. We have described the properties of the 2.4 Hz mode in Section 3 and shown in Section 6 that its energy of the is critical for the results of the ACs, as the gathers and stacks drastically change when the mode is excluded (compare Figs. 9 & 16). For this reason it is inevitable to know the origin of this signal and whether it should be excluded for ambient noise studies or whether it can be used a source.
The 2.4 Hz mode is present through the entire Martian evening period and seems not to be affected significantly by the wind or temperature. Its generation mechanism is still a subject of ongoing debate within the scientific community and its origin is not clear up to now. There are currently three main working hypothesis being investigated by the scientific teams (*Kim* et al., 2021; *Hobiger* et al., 2021):

1. it is a resonance of a local subsurface structure below the lander (e.g. *Giardini* et al., 2020; *Dahmen* et al., 2021)

2. it is a resonance of the lander related to its solar panels

3. it is is energy trapped in the subsurface related to surface waves (*Hobiger* et al., 2021)

Its stability and independence from wind and surface temperature favors the first case, which makes it a suitable source for ambient noise autocorrelation. However, we can not rule out the other generation mechanism. *Hobiger* et al. (2021) inverted Rayleigh wave ellipticity curves, extracted from the ambient noise vibrations, and proposed the origin of the 2.4 Hz mode as an Airy phase, that is related to surface wave energy, trapped in local low velocity layer between 30-75 m depth. They proposed, that this low velocity layer represents a sedimentary layer overlain by basalts. If future work will confirm these results in the sense that the 2.4 Hz mode is indeed related to surface waves, then it has to be removed from the data before computing the ACs. Hence, our results and the results from previous studies (e.g. *Compaire* et al., 2021; *Deng* and *Levander*, 2020; *Schimmel* et al., 2021) would have to be re-assessed as they are mostly relying on the energy of the 2.4 Hz mode. However, a question arises with the hypothesis of the 2.4 Hz being induced by surface waves: how do surface wave generate this spectral shape of the 2.4 Hz mode resulting in the periodic pattern in the ACs?

7.3 Comparison of Results with Previous Studies

The first results of ACs from the SEIS data were shown by *Suemoto* et al. (2020). They focussed their study on the shallow structures using only high frequencies between 5-7 Hz and obtained arrivals at 0.6 and 1.1 s in the ACs. However, as this band is contaminated by a strong lander mode at $\sim$6.8 Hz that maps into the early lag times of the ACs, their results need to be re-assessed after removing the mode from the data (*Kim* et al., 2021). The first potential arrivals from deeper crustal and mantle structures were presented by *Deng* and *Levander* (2020), using the moving average amplitude balancing after *Bensen* et al. (2007) and phase weighted stacking of the vertical ACs. They obtain arrivals at $\sim$11.5

and ∼21.0 s for different bands between 0.625 and 3 Hz (see Fig. 2 in *Deng* and *Levander*, 2020) that they interpret as P- and S-wave reflections from the Moho. They further show later arrivals at ∼280 and ∼375 s in different bands from 0.05-0.2 Hz, that they interpret as reflections from the Olivine-Wadsleyite Transition within the lower mantle and the core-mantle boundary, respectively. However, the authors did not deglitch the data prior to their analysis and these late arrivals could not be reproduced on a deglitched dataset, whereas they were obtained, using glitch-contaminated data (*Kim* et al., 2021).
A study from *Compaire* et al. (2021) revealed distict arrivals in the ACs at 5.6, 10.6, 12.6 and 21.0 s in the 1-3 Hz band on the vertical component (see Fig. 9 in *Compaire* et al., 2021). They deticked and deglitched the data, applied a one-bit amplitude normalization and used three independent methods, AACs, MACs and the Welch method (*Welch*, 1967), before linear stacking. All three methods agree in their declared arrivals. In another study, *Schimmel* et al. (2021) selected data windows with respect to the RMS amplitude, which essentially filters out parts of the data, that contain many transient signals of large amplitude (e.g. glitches). They further apply time-frequency weighted stacking and filter the ACs in different bands. Finally, they retrieve the same 10.6 s arrival in two of three bands (see Fig. 11 in *Schimmel* et al., 2021). They did not deglitch the data prior to their analysis but, as shown by *Compaire* et al. (2021) and discussed before, this should not have strong impact on the earlier lag times. Finally, *Kim* et al. (2021) studied the potential pitfalls of the AC analysis that rise from spurious signals (e.g. glitches, ticknoise) and landermodes and compiles the results from previous studies.
On the vertical component we obtain the same arrivals as *Compaire* et al. (2021) at ∼10.8, ∼12.7 and ∼20.8 s.*Deng* and *Levander* (2020) did not distinguish between the energy of the first two mentioned arrivals and picked them as one at ∼11.5 s. They also obtained the arrival at ∼21 s. Furthermore, the three arrivals are stable over both methods, AACs and the MACs, as shown in Section 6. *Compaire* et al. (2021) also computed the ACs for the north and east components. For the north component they obtain arrivals at 11.9, 14.4, 16.5 and 22.4 s lag time (see Fig. 9 in *Compaire* et al., 2021). With arrival times of 12.1, 16.5 and 22.6 s, our results agree here as well (Fig.15). However, the arrival at ∼14.4 is not obvious and we thus did not pick it. For the east component *Compaire* et al. (2021) determined arrivals at 9, 12.4 and 14.5 s (Fig. 8 in *Compaire* et al., 2021). Here their second arrival agrees with the arrival we observe at 12.4 (Fig.15). As stated before we excluded the energy at ∼9 s from the analysis and we do not see their third arrival at 14.5 s. Instead, we observe an arrival at 17 s, which is though only observed on the AACs and thus less trustworthy. All in all, our results from both, AACs and MACs, agree very well with the results from other studies within uncertainties of mostly less than ∼0.5 s. In comparison to *Compaire* et al. (2021) (1-3 Hz) we extended the used bandwidth to both the lower and higher frequencies (0.3-8.5 Hz). Though, the obtained ACs did not change much as the band beyond the 2.4 Hz mode only has a minor effect on the ACs, in fact is almost negligible on the vertical component.

7.4 Potential Layer Interfaces

Recently, *Knapmeyer-Endrun* et al. (2021) computed P-S converted receiver functions for three marsquakes with high SNR of the P-phase as well as determined back azimuths, and inverted these phases for a subsurface layer model. Over a variety of different methods,

they found consistent phases at ∼2.4, ∼4.8 and ∼7.5 s, where the first two correspond to layer depths of 6-11 and 15-25 km, respectively. Interpreting these arrivals as converted phases from the crust-mantle boundary (Moho) results in a local crustal thickness below the lander of either 15-25 or 27-47 km, respectively (*Knapmeyer-Endrun* et al., 2021). The first phase thereby reveals upper layer S-wave velocities of 1.2-2.1 km/s, that agree with the velocities reported by *Lognonné* et al. (2020). The inferred upper layer interface is also supported by computed S-P conversion phases (*Knapmeyer-Endrun* et al., 2021). The obtained arrivals on the vertical component and their corresponding lag times at ∼11 and ∼21 s from our ACs are consistent with the arrivals from other studies using AC analysis ((*Compaire* et al., 2021; *Schimmel* et al., 2021; *Deng* and *Levander*, 2020). We interpret them as trapped P-waves that are reflected between layer interfaces and the surface. We use the range of inferred crustal S-wave velocities and Vp/Vs ratios provided by *Lognonné* et al. (2020)(Table S3 in *Lognonné* et al., 2020) and obtain P-wave velocities of 3.5-5.2 km/s. Using these velocities, the picked arrival times, 10.8 and 12.7 s , which correspond to two-way traveltime, yield depths of the potential layer interface (e.g. the Moho) between 19-28 km and 22-33 km, respectively. These results are consistent with the inference from the receiver functions (*Knapmeyer-Endrun* et al., 2021). *Deng* and *Levander* (2020) interpreted the ∼10 and ∼21 s arrivals as subsequent P- and S-wave reflection from the Moho, respectively. However, as a vertically propagating S-wave is polarized in the horizontal components and the arrival is observed on the vertical component, it is more likely that the ∼21 s arrival is a multiple reflection of the first phase (*Knapmeyer-Endrun* et al., 2021). Conversely, *Compaire* et al. (2021) obtained an amplitude ratio of 1.5-2 between the first arrival in the ACs and the later arrivals 21 s and argue that it is unlikely that these later arrivals are multiples of the earlier ones. Using the same Vp/Vs ratio as before we would expect the corresponding S-wave arrivals on the horizontal components at lag times of 17.3-22.7 s and 20.3-26.7 s for the 10.8 and 12.7 s P-wave arrivals, respectively. Interestingly, our obtained arrivals on the north component, at 16.5 and 22.6 s almost fall within the range of the expected S-wave arrivals. Another candidate is the arrival at 17.0 s on the east component, although it is only obtained through the AACs and thus less trustworthy.

8 Conclusion and Outlook

In this study we have processed over one year of the SEIS VBB 20 sps data, suppressed the ticknoise, the glitches and the lander modes. We then computed both the ambient noise autocorrelations for the evening and early night times of the most stable part of the acquisition period (sols 180-550) and 250 marsquake autocorrelations for intermediate and high quality high frequency events. The autocorrelograms of both methods agree very well and show distinct arrivals, that can be interpreted as trapped P- and S-waves on the vertical and horizontal components, respectively. These trapped waves are assumed to be reflected phases that reverberate between then surface and layer interfaces in the subsurface. With the good agreement in arrival times our results further confirm the results from previous studies on ambient noise autocorrelation of SEIS data (e.g. *Deng* and *Levander*, 2020; *Compaire* et al., 2021; *Schimmel* et al., 2021). Here, the obtained arrival times of the vertical component, namely at 10.8 and 12.7, could present reflections from the Moho and are converted to depth range of 19-28 or 22-33 km, respectively, using

a mean crustal velocity of 3.5-5.2 km/s. We further retrieve arrivals on the horizontal components at 16.5 and 22.6 s (north) and 17.0 s (east), that may be the corresponding S-wave composites of the reflected P-phases.

Moreover, we show that the results of the autocorrelations are almost entirely depending on the energy of the 2.4 Hz mode. Suppressing the 2.4 Hz mode changes the AC results drastically and the previously obtained arrivals can no longer be identified. Authors of previous studies have assumed that the 2.4 Hz mode can be considered as a subsurface resonance, that can be used as a source for ambient noise autocorrelation to resolve the subsurface reflectivity below the lander. However, recently *Hobiger* et al. (2021) challenged this view and proposed an origin of the 2.4 Hz mode related to surface wave energy trapped in a low velocity zone below the lander. Future work needs to further investigate the 2.4 Hz mode and its origin as it is absolutely critical for the ambient noise analysis on SEIS data. If the hypothesis of *Hobiger* et al. (2021) will be confirmed and the 2.4 Hz mode is indeed generated by surface waves, it has to be removed before any AC analysis. In that case, our results and the results from the discussed previous ambient noise studies would need to be re-assessed.

Acknowledgements

All InSight data can be accessed through IRIS (`https://www.iris.edu/hq/sis/insight`; *IRIS: Incorporated Research Institutions for Seismology*, 2020) or NASAs PDS archive(https://pds-geosciences.wustl.edu/missions/insight/index.htm). We are very grateful for the very helpful advice and guidance regarding the SEIS & APSS data and the marsquake catalogue from Dr. Savas Ceylan from the Marsquake Service. We also want to thank Dr. Heinrich Horstmeyer from ETH Zürich (Institute of Geophysics) for the very helpful support on remote access computing and software setup. We further thank Prof. Dr. Giardini and the entire Mars Team from ETH Zürich for insightful discussions.
The data processing flow is coded with Python (*Van Rossum* and *Drake Jr*, 1995; *Oliphant*, 2007) and heavily relies on the libraries Numpy (*Oliphant*, 2006) and SciPy (*Virtanen* et al., 2020). For the reading, processing and writing of the SEIS data we use the seismological Python package ObsPy (*Beyreuther* et al., 2010b; *Krischer* et al., 2015). All figures are created with Matplotlib (*Hunter*, 2007).

References

Banerdt, WB, SE *Smrekar*, D *Banfield*, D *Giardini*, M *Golombek*, CL *Johnson*, P *Lognonné*, A *Spiga*, T *Spohn*, C *Perrin*, et al. (2020). "Initial results from the InSight mission on Mars". In: *Nature Geoscience* 13.3. DOI: https://doi.org/10.1038/s41561-020-0544-y.

Banfield, D, JA *Rodriguez-Manfredi*, CT *Russell*, KM *Rowe*, D *Leneman*, HR *Lai*, PR *Cruce*, JD *Means*, CL *Johnson*, A *Mittelholz*, et al. (2019). "InSight auxiliary payload sensor suite (APSS)". In: *Space Science Reviews* 215.1, pp. 1–33. DOI: https://doi.org/10.1007/s11214-018-0570-x.

Baratoux, David, Michael J *Toplis*, Marc *Monnereau*, and Olivier *Gasnault* (2011). "Thermal history of Mars inferred from orbital geochemistry of volcanic provinces". In: *Nature* 472.7343, pp. 338–341. DOI: https://doi.org/10.1038/nature09903.

Bensen, GD, MH *Ritzwoller*, MP *Barmin*, A Lin *Levshin*, Feifan *Lin*, MP *Moschetti*, NM *Shapiro*, and Yanyan *Yang* (2007). "Processing seismic ambient noise data to obtain reliable broad-band surface wave dispersion measurements". In: *Geophysical Journal International* 169.3, pp. 1239–1260. DOI: https://doi.org/10.1111/j.1365-246X.2007.03374.x.

Beyreuther, Moritz, Robert *Barsch*, Lion *Krischer*, Tobias *Megies*, Yannik *Behr*, and Joachim *Wassermann* (2010a). "ObsPy: A Python toolbox for seismology". In: *Seismological Research Letters* 81.3, pp. 530–533. DOI: https://doi.org/10.1785/gssrl.81.3.530.

— (2010b). "ObsPy: A Python toolbox for seismology". In: *Seismological Research Letters* 81.3, pp. 530–533. DOI: https://doi.org/10.1785/gssrl.81.3.530.

Campillo, Michel and Anne *Paul* (2003). "Long-range correlations in the diffuse seismic coda". In: *Science* 299.5606, pp. 547–549. DOI: https://doi.org/10.1126/science.1078551.

Ceylan, Savas, John F *Clinton*, Domenico *Giardini*, Maren *Böse*, Constantinos *Charalambous*, Martin van *Driel*, Anna *Horleston*, Taichi *Kawamura*, Amir *Khan*, Guenolé *Orhand-Mainsant*, et al. (2020). "Companion guide to the marsquake catalog from InSight, Sols 0–478: Data content and non-seismic events". In: *Physics of the Earth and Planetary Interiors*, p. 106597. DOI: https://doi.org/10.1016/j.pepi.2020.106597.

Claerbout, Jon F (1968). "Synthesis of a layered medium from its acoustic transmission response". In: *Geophysics* 33.2, pp. 264–269. DOI: https://doi.org/10.1190/1.1439927.

Clinton, John F, Savas *Ceylan*, Martin van *Driel*, Domenico *Giardini*, Simon C *Stähler*, Maren *Böse*, Constantinos *Charalambous*, Nikolaj L *Dahmen*, Anna *Horleston*, Taichi *Kawamura*, et al. (2021). "The Marsquake catalogue from InSight, sols 0–478". In: *Physics of the Earth and Planetary Interiors* 310, p. 106595. DOI: https://doi.org/10.1016/j.pepi.2020.106595.

Compaire, Nicolas, Ludovic *Margerin*, Raphaël F *Garcia*, Baptiste *Pinot*, Marie *Calvet*, Guénolé *Orhand-Mainsant*, Doyeon *Kim*, Vedran *Lekic*, Benoit *Tauzin*, Martin *Schimmel*, et al. (2021). "Autocorrelation of the Ground Vibrations Recorded by the SEIS-InSight Seismometer on Mars". In: *Journal of Geophysical Research: Planets* 126.4, e2020JE006498. DOI: https://doi.org/10.1029/2020JE006498.

Dahmen, Nikolaj L, John F *Clinton*, Savas *Ceylan*, Martin van *Driel*, Domenico *Giardini*, Amir *Khan*, Simon C *Stähler*, Maren *Böse*, Constantinos *Charalambous*, Anna *Horleston*, et al. (2020). "Super high frequency events: a new class of events recorded by the InSight seismometers on Mars". In: *Journal of Geophysical Research: Planets*, e2020JE006599. DOI: https://doi.org/10.1029/2020JE006599.

Dahmen, Nikolaj L, Géraldine. *Zenhäusern*, John F *Clinton*, Domenico *Giardini*, Simon C *Stähler*, Savas *Ceylan*, Constantinos *Charalambous*, Martin van *Driel*, J. Hurst *Kenneth*, Sharon *Kedar*, Philippe *Lognonné*, *Murdoch*, et al. (2021). "Resonances and Lander Modes obserbed by InSight on Mars (1-9 Hz)". In: *Bulletin of Seismological Society of America. Submitted.*

Deng, Sizhuang and Alan *Levander* (2020). "Autocorrelation reflectivity of Mars". In: *Geophysical Research Letters* 47.16, e2020GL089630. DOI: https://doi.org/10.1029/2020GL089630.

Driel, Martin van, Savas *Ceylan*, John F *Clinton*, Domenico *Giardini*, Anna *Horleston*, Ludovic *Margerin*, Simon C *Stähler*, Maren *Böse*, Constantinos *Charalambous*, Taichi *Kawamura*, et al. (2021). "High-frequency seismic events on Mars observed by InSight". In: *Journal of Geophysical Research: Planets* 126.2, e2020JE006670. DOI: https://doi.org/10.1029/2020JE006670.

Edme, Pascal and David F *Halliday* (2016). "Near-surface imaging using ambient-noise body waves". In: *Interpretation* 4.3, SJ55–SJ65. DOI: https://doi.org/10.1190/INT-2016-0002.1.

Galetti, Erica and Andrew *Curtis* (2012). "Generalised receiver functions and seismic interferometry". In: *Tectonophysics* 532, pp. 1–26. DOI: https://doi.org/10.1016/j.tecto.2011.12.004.

Giardini, Domenico, Philippe *Lognonné*, William Bruce *Banerdt*, William T *Pike*, Ulrich *Christensen*, Savas *Ceylan*, John Francis *Clinton*, Martin van *Driel*, Simon C *Stähler*, Maren *Böse*, et al. (2020). "The seismicity of Mars". In: *Nature Geoscience* 13.3, pp. 205–212. DOI: https://doi.org/10.1038/s41561-020-0539-8.

Golombek, Matthew, D *Kipp*, N *Warner*, Ingrid J *Daubar*, R *Fergason*, Randolph L *Kirk*, R *Beyer*, A *Huertas*, Sylvain *Piqueux*, NE *Putzig*, et al. (2017). "Selection of the InSight landing site". In: *Space Science Reviews* 211.1, pp. 5–95. DOI: https://doi.org/10.1007/s11214-016-0321-9.

Golombek, Matthew, NH *Warner*, JA *Grant*, Ernst *Hauber*, V *Ansan*, CM *Weitz*, Nathan *Williams*, C *Charalambous*, SA *Wilson*, A *DeMott*, et al. (2020). "Geology of the InSight landing site on Mars". In: *Nature Communications* 11.1, pp. 1–11. DOI: https://doi.org/10.1038/s41467-020-14679-1.

Gorbatov, Alexei, Erdinc *Saygin*, and BLN *Kennett* (2013). "Crustal properties from seismic station autocorrelograms". In: *Geophysical Journal International* 192.2, pp. 861–870. DOI: https://doi.org/10.1093/gji/ggs064.

Harris, Fredric J (1978). "On the use of windows for harmonic analysis with the discrete Fourier transform". In: *Proceedings of the IEEE* 66.1, pp. 51–83. DOI: https://doi.org/10.1109/PROC.1978.10837.

Hobiger, M., M. *Hallo*, C. *Schmelzbach*, Simon C *Stähler*, D. *Faeh*, Domenico *Giardini*, et al. (2021). "The shallow structure of Mars from inversion of high-frequency ambient seismic vibrations Rayleigh wave ellipticity at the InSight landing site". In: *Bulletin of Seismological Society of America. Submitted.*

Hodgson, Murray (1996). "When is diffuse-field theory applicable?" In: *Applied Acoustics* 49.3, pp. 197–207. DOI: https://doi.org/10.1016/S0003-682X(96)00010-2.

Hunter, John D (2007). "Matplotlib: A 2D graphics environment". In: *Computing in science & engineering* 9.03, pp. 90–95. DOI: https://doi.org/10.1109/MCSE.2007.55.

Insight Mars SEIS Data Service (2019). "SEIS raw data, Insight Mission". In: DOI: https://doi.org/10.18715/SEIS.INSIGHT.XB_2016.

InSight Marsquake Service (2021). *Mars Seismic Catalogue, InSight Mission; V6 2021-04-01*. en. DOI: https://doi.org/10.12686/a11. URL: https://www.insight.ethz.ch/seismicity/catalog/v6.

IRIS: Incorporated Research Institutions for Seismology (2020). "NASA's Insight Mission". In: URL: https://www.iris.edu/hq/sis/insight (visited on 01/24/2021).

Kim, D., P. *Davis*, V. *Lekic*, R. *Maguire*, N. *Compaire*, M. *Schimmel*, et al. (2021). "Potential Pitfalls in the Analysis and Structural Interpretation of Mars Seismic Data from Insight". In: *JGR: Planets ???. Submitted.*

Knapmeyer-Endrun, Brigitte, Mark P *Panning*, Felix *Bissig*, Rakshit *Joshi*, Amir *Khan*, Doyeon *Kim*, Vedran *Lekić*, Benoit *Tauzin*, Saikiran *Tharimena*, Matthieu *Plasman*, et al. (2021). "Thickness and structure of the martian crust from InSight seismic data". In: *Science* 373.6553, pp. 438–443. DOI: https://doi.org/10.1126/science.abf8966.

Krischer, Lion, Tobias *Megies*, Robert *Barsch*, Moritz *Beyreuther*, Thomas *Lecocq*, Corentin *Caudron*, and Joachim *Wassermann* (2015). "ObsPy: A bridge for seismology into the scientific Python ecosystem". In: *Computational Science & Discovery* 8.1, p. 014003. DOI: http://dx.doi.org/10.1088/1749-4699/8/1/014003.

Lobkis, Oleg I and Richard L *Weaver* (2001). "On the emergence of the Green's function in the correlations of a diffuse field". In: *The Journal of the Acoustical Society of America* 110.6, pp. 3011–3017. DOI: https://doi.org/10.1121/1.1417528.

Lognonné, Philippe, W Bruce *Banerdt*, D *Giardini*, WT *Pike*, U *Christensen*, P *Laudet*, S *De Raucourt*, P *Zweifel*, S *Calcutt*, Marco *Bierwirth*, et al. (2019). "SEIS: Insight's seismic experiment for internal structure of Mars". In: *Space Science Reviews* 215.1. DOI: https://doi.org/10.1007/s11214-018-0574-6.

Lognonné, Philippe, WB *Banerdt*, WT *Pike*, Domenico *Giardini*, U *Christensen*, Raphaël F *Garcia*, T *Kawamura*, S *Kedar*, B *Knapmeyer-Endrun*, L *Margerin*, et al. (2020). "Constraints on the shallow elastic and anelastic structure of Mars from InSight seismic data". In: *Nature Geoscience* 13.3, pp. 213–220. DOI: https://doi.org/10.1038/s41561-020-0536-y.

Mulargia, Francesco (2012). "The seismic noise wavefield is not diffuse". In: *The Journal of the Acoustical Society of America* 131.4, pp. 2853–2858. DOI: https://doi.org/10.1121/1.3689551.

NASA (2021a). "Insight Mission, Mars". In: URL: https://mars.nasa.gov/insight/spacecraft/instruments/ (visited on 01/17/2021).

— (2021b). "Insight Mission, Mars". In: URL: https://mars.nasa.gov/news/8959/nasas-insight-mars-lander-gets-a-power-boost/?site=insight (visited on 08/01/2021).

Nishitsuji, Yohei, Charlotte Anne *Rowe*, Kees *Wapenaar*, and Deyan *Draganov* (2016). "Reflection imaging of the Moon's interior using deep-moonquake seismic interferom-

etry". In: *Journal of Geophysical Research: Planets* 121.4, pp. 695–713. DOI: https://doi.org/10.1002/2015JE004975.

Oliphant, Travis E (2006). *A guide to NumPy*. Vol. 1. Trelgol Publishing USA.

— (2007). "Python for scientific computing". In: *Computing in science & engineering* 9.3, pp. 10–20. DOI: https://doi.org/10.1109/MCSE.2007.58.

Oren, Can and Robert L *Nowack* (2016). "Seismic body-wave interferometry using noise auto-correlations for crustal structure". In: *Geophysical Journal International*, ggw394. DOI: https://doi.org/10.1093/gji/ggw394.

Panning, Mark P, W Tom *Pike*, Philippe *Lognonné*, W Bruce *Banerdt*, Naomi *Murdoch*, Don *Banfield*, Constantinos *Charalambous*, Sharon *Kedar*, Ralph D *Lorenz*, Angela G *Marusiak*, et al. (2020). "On-deck seismology: Lessons from InSight for future planetary seismology". In: *Journal of Geophysical Research: Planets* 125.4, e2019JE006353. DOI: https://doi.org/10.1029/2019JE006353.

Pham, Thanh-Son and Hrvoje *Tkalčić* (2017). "On the feasibility and use of teleseismic P wave coda autocorrelation for mapping shallow seismic discontinuities". In: *Journal of Geophysical Research: Solid Earth* 122.5, pp. 3776–3791. DOI: https://doi.org/10.1002/2017JB013975.

Savoie, Denis, Andy *Richard*, Marc *Goutaudier*, P *Lognonné*, KJ *Hurst*, Justin N *Maki*, Matthew P *Golombek*, Martin van *Driel*, John *Clinton*, Eleonore *Stutzmann*, et al. (2021). "Finding SEIS North on Mars: Comparisons between SEIS sundial, Inertial and Imaging measurements and consequences for seismic analysis". In: *Earth and Space Science* 8.3, e2020EA001286. DOI: https://doi.org/10.1029/2020EA001286.

Schimmel, Martin and Hanneke *Paulssen* (1997). "Noise reduction and detection of weak, coherent signals through phase-weighted stacks". In: *Geophysical Journal International* 130.2, pp. 497–505. DOI: https://doi.org/10.1111/j.1365-246X.1997.tb05664.x.

Schimmel, Martin, Eleonore *Stutzmann*, Philippe *Lognonné*, Nicolas *Compaire*, Paul *Davis*, Melanie *Drilleau*, Raphael *Garcia*, Doyeon *Kim*, Brigitte *Knapmeyer-Endrun*, Vedran *Lekic*, et al. (2021). "Seismic Noise Autocorrelations on Mars". In: *Earth and Space Science*, e2021EA001755. DOI: https://doi.org/10.1029/2021EA001755.

Scholz, John-Robert, Rudolf *Widmer-Schnidrig*, Paul *Davis*, Philippe *Lognonné*, Baptiste *Pinot*, Raphaël F *Garcia*, Kenneth *Hurst*, Laurent *Pou*, Francis *Nimmo*, Salma *Barkaoui*, et al. (2020). "Detection, analysis, and removal of glitches from InSight's seismic data from Mars". In: *Earth and Space Science* 7.11, e2020EA001317. DOI: https://doi.org/10.1029/2020EA001317.

Smrekar, Suzanne E, Philippe *Lognonné*, Tilman *Spohn*, W Bruce *Banerdt*, Doris *Breuer*, Ulrich *Christensen*, Véronique *Dehant*, Mélanie *Drilleau*, William *Folkner*, Nobuaki *Fuji*, et al. (2019). "Pre-mission InSights on the interior of Mars". In: *Space Science Reviews* 215.1, pp. 1–72. DOI: https://doi.org/10.1007/s11214-018-0563-9.

Snieder, Roel (2004). "Extracting the Green's function from the correlation of coda waves: A derivation based on stationary phase". In: *Physical Review E* 69.4, p. 046610. DOI: https://doi.org/10.1103/PhysRevE.69.046610.

Spiga, Aymeric, Naomi *Murdoch*, Ralph *Lorenz*, François *Forget*, Claire *Newman*, Sébastien *Rodriguez*, Jorge *Pla-Garcia*, D Viúdez *Moreiras*, Don *Banfield*, Clément *Perrin*, et al. (2021). "A study of daytime convective vortices and turbulence in the martian Planetary Boundary Layer based on half-a-year of InSight atmospheric measurements

and Large-Eddy Simulations". In: *Journal of Geophysical Research: Planets* 126.1, e2020JE006511. DOI: https://doi.org/10.1029/2020JE006511.

Stutzmann, E, Martin *Schimmel*, Philippe *Lognonné*, Anna *Horleston*, Savas *Ceylan*, Martin van *Driel*, Simon *Stahler*, Bruce *Banerdt*, Marie *Calvet*, Constantinos *Charalambous*, et al. (2021). "The polarization of ambient noise on Mars". In: *Journal of Geophysical Research: Planets* 126.1, e2020JE006545. DOI: https://doi.org/10.1029/2020JE006545.

Suemoto, Yudai, Tatsunori *Ikeda*, and Takeshi *Tsuji* (2020). "Temporal variation and frequency dependence of seismic ambient noise on Mars from polarization analysis". In: *Geophysical Research Letters* 47.13, e2020GL087123. DOI: https://doi.org/10.1029/2020GL087123.

Van Rossum, Guido and Fred L *Drake Jr* (1995). *Python reference manual*. Centrum voor Wiskunde en Informatica Amsterdam.

Virtanen, Pauli, Ralf *Gommers*, Travis E *Oliphant*, Matt *Haberland*, Tyler *Reddy*, David *Cournapeau*, Evgeni *Burovski*, Pearu *Peterson*, Warren *Weckesser*, Jonathan *Bright*, et al. (2020). "SciPy 1.0: fundamental algorithms for scientific computing in Python". In: *Nature methods* 17.3, pp. 261–272. DOI: https://doi.org/10.1038/s41592-019-0686-2.

Wapenaar, Kees (2003). "Synthesis of an inhomogeneous medium from its acoustic transmission response". In: *Geophysics* 68.5, pp. 1756–1759. DOI: https://doi.org/10.1190/1.1620649.

— (2004). "Retrieving the elastodynamic Green's function of an arbitrary inhomogeneous medium by cross correlation". In: *Physical review letters* 93.25, p. 254301. DOI: https://doi.org/10.1103/PhysRevLett.93.254301.

Weaver, Richard L and Oleg I *Lobkis* (2005). "Fluctuations in diffuse field–field correlations and the emergence of the Green's function in open systems". In: *The Journal of the Acoustical Society of America* 117.6, pp. 3432–3439. DOI: https://doi.org/10.1121/1.1898683.

Welch, Peter (1967). "The use of fast Fourier transform for the estimation of power spectra: a method based on time averaging over short, modified periodograms". In: *IEEE Transactions on audio and electroacoustics* 15.2, pp. 70–73. DOI: https://doi.org/10.1109/TAU.1967.1161901.

Zweifel, P et al. (2021). "Seismic High-Resolution Acquisition Electronics for the NASA InSight mission on Mars". In: *Bulletin of Seismological Society of America. In preparation.*

Appendix

Here, we briefly go through the 1D derivations from *Wapenaar* (2003): The wavefield can be artificially subdivided into an up- and downgoing wavefield. We stick to the notation of *Wapenaar* (2003) and use an $U(\omega)$ for the upgoing and $D(\omega)$ for the downgoing wavefield in the frequency domain. Figure A1 illustrates a sketch of a layered medium and the wavefield with its subdivision into the reflected field (R) and the transmitted field (T). Below the free surface the up- and downgoing wavefields are defined as:

$$D = 1 - R, U = R \tag{5}$$

such that the total powerflux is given by:

$$D^*D - U^*U = (1 - R^*)(1 - R) - R^*R = 1 - R - R^* \tag{6}$$

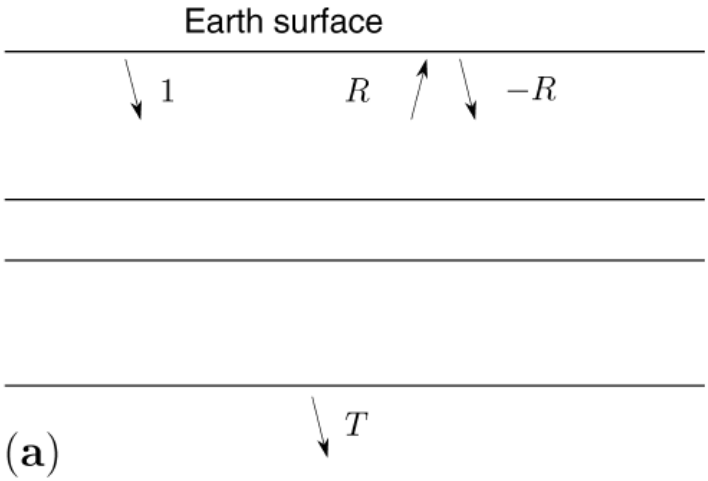

Figure A1: Conceptual sketch of the wavefield subdivision into reflection and transmission response for a simplified layered medium from *Wapenaar* (2003).

Below the lowest layer interface we assume a homogeneous halfspace and hence neglect any reflected energy below that boundary. Thus the downgoing powerflux of the wavefield below the lowest boundary is only given by the transmission response $T(\omega)$:

$$D^*D - U^*U = D^*D = T^*T \tag{7}$$

Assuming the conservation of power flux ($D^*D - U^*U$) we can equalize Equations 8 and 8:

$$R(\omega) + R^*(\omega) = 1 - T^*(\omega)T(\omega) \tag{8}$$

which corresponds to the following expression in the time domain:

$$R(t) + R(-t) = \delta(t) - T(-t) * T(t) \tag{9}$$

where the $*$ denotes the convolution operator. Since the reflectivity is defined to be a causal signal, the acausal part can be neglected. As $T(-t) * T(t)$ represents the autocorrelation function of $T(t)$, we can deduce, that the reflectivity can be derived from the autocorrelation of the transmission response of an impulse source ($\delta(t)$). *Wapenaar* (2003) further notes, that as the AC is not affected by the source, the derivation is valid for any source, which still yields an AC of an impulsive nature. Thus, ambient white noise can be used as a source to retrieve the reflectivity. The only requirement is the location of the source, outside of the observed layered medium, and hence within the halfspace below the lowest layer boundary.

Supplementary Material

Supplementary Figures and Tables

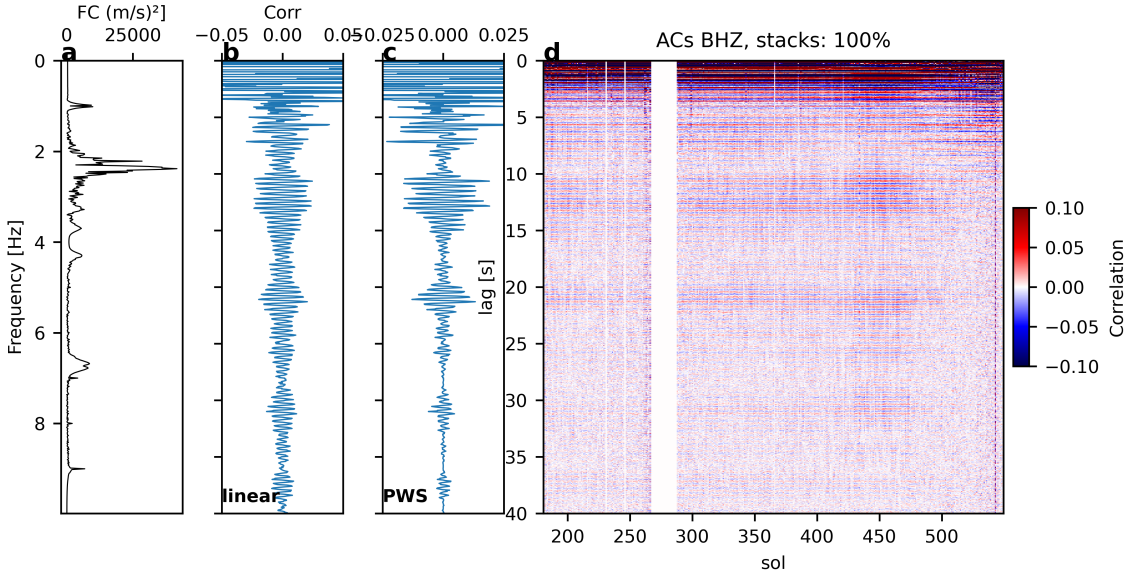

Figure S1: (a) Spectra, (b) linear stack (c) PWS and (d) AC gather for the brute AC computation of the vertical component not using any attribute filtering. All 100% of the considered data windows are used. Both the AC gather as well as the stacks are normalized by their maximum at the zero lag and clipped.

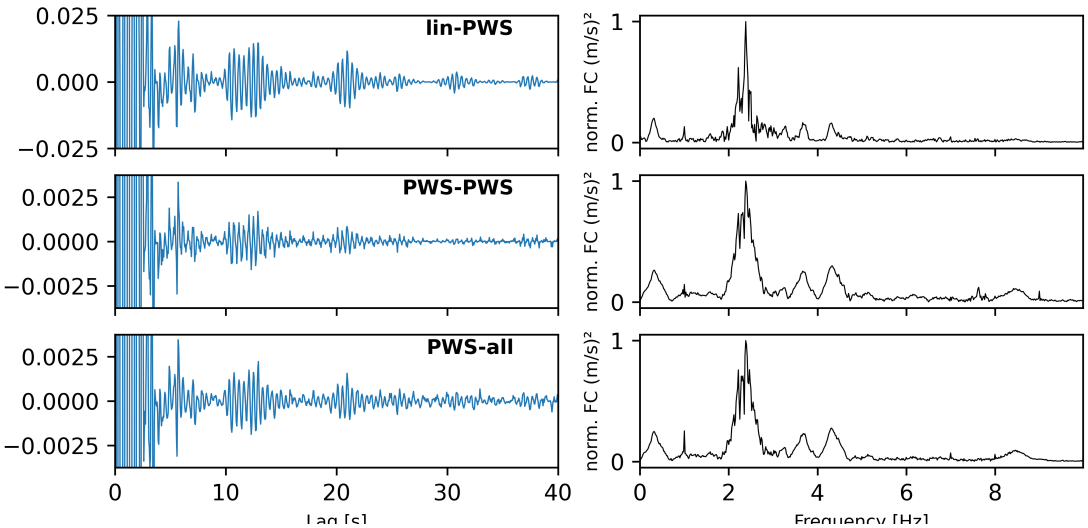

Figure S2: Compilation of different PWS computation approaches for the vertical component, discussed in Section 5

.

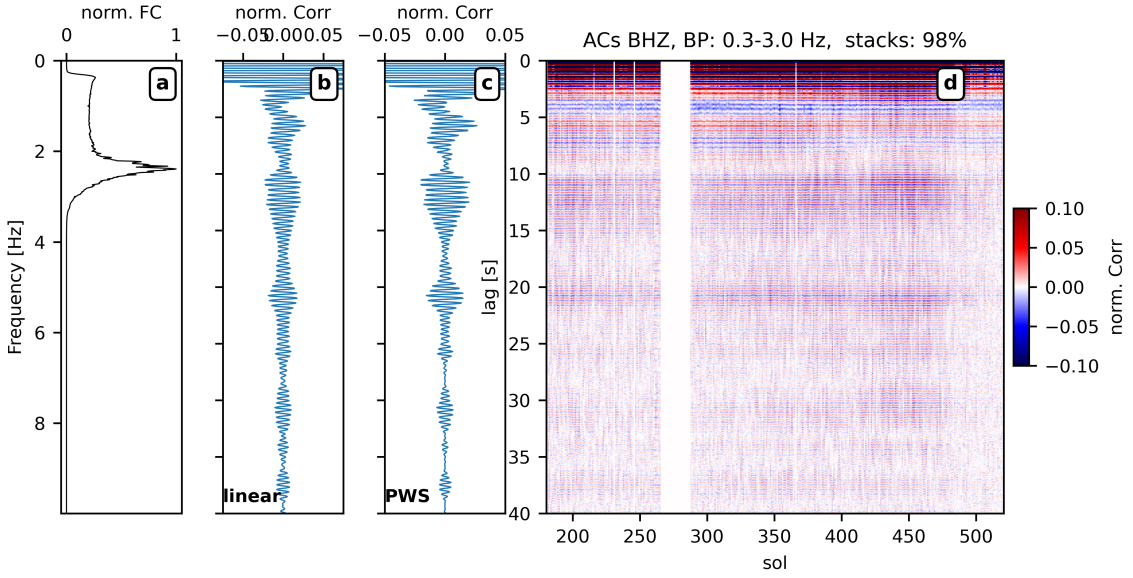

Figure S3: Same as Figure 9 but bandpass filtered between 0.3-3.2 Hz to exclude any potential contamination by lander modes.

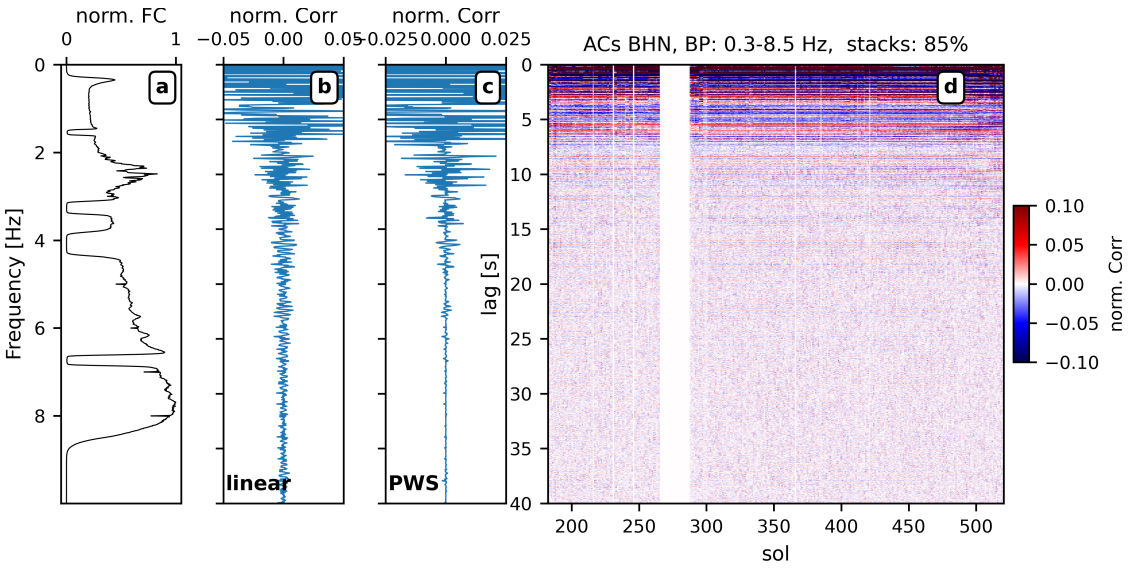

Figure S4: Same as Figure 9 but for the north component. Here, 85 % of the considered data windows are used. Note the stronger clipping compared to the vertical component.

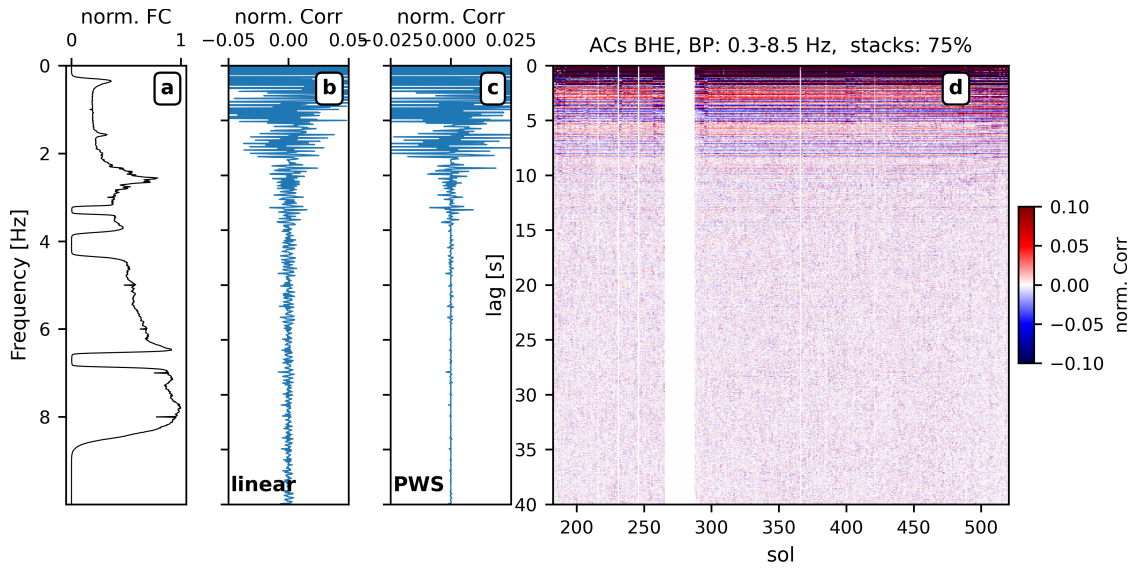

Figure S5: Same as Figure 9 but for the east component. Here, 75% of the considered data windows are used. Note the stronger clipping compared to the vertical component.

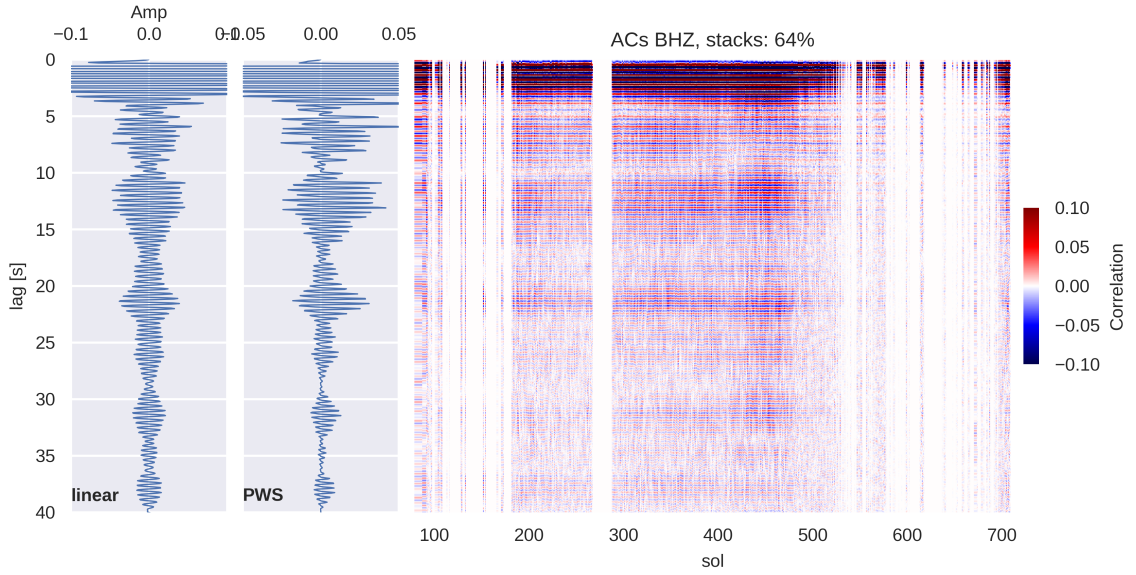

Figure S6: ACs for the entire data set from sol 82 to sol 710, for the vertical component. Here, the wind data is not considered in the evaluation. Only 64% of the data windows are used while the rest is rejected for exceeding the wind and late amplitude thresholds.

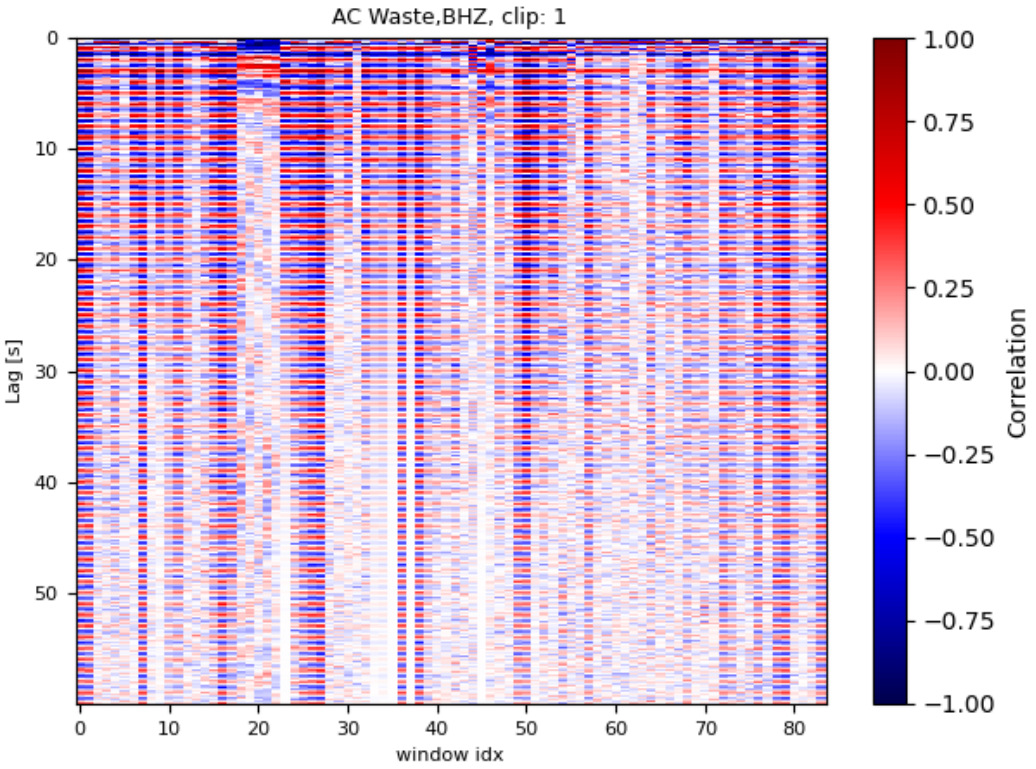

Figure S7: Vertical componenten ACs that are rejected by exceeding the amplitude threshold of 25 % of the zero lag for lag times greater than 10 s.

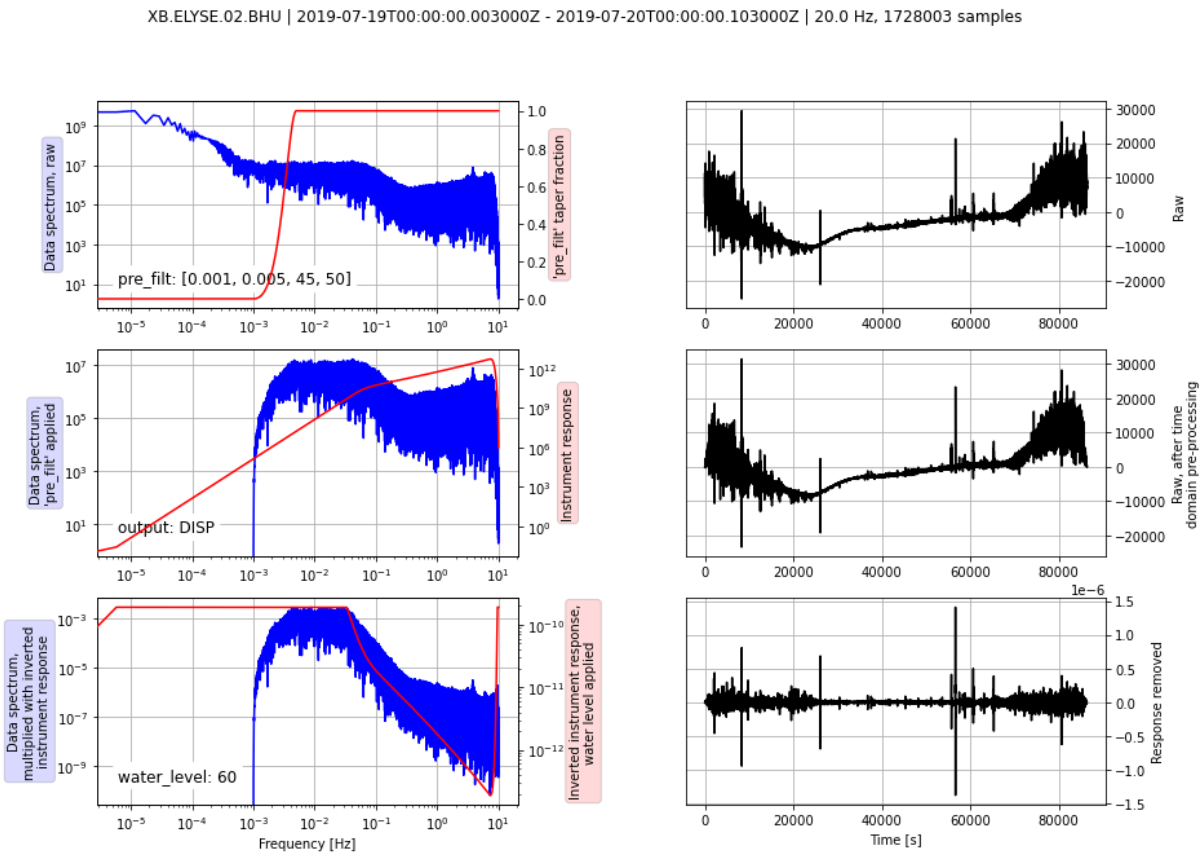

Figure S8: Procedure of the instrument response removal for component U of the exemplary Earth day 200 of 2019.